Tropical Thermodynamic–Convection Coupling in Observations and Reanalyses

BRANDON WOLDING,[a,b] SCOTT W. POWELL,[c] FIAZ AHMED,[d] JULIANA DIAS,[e] MARIA GEHNE,[a,b] GEORGE KILADIS,[e] AND J. DAVID NEELIN[d]

[a] *Cooperative Institute for Research in Environmental Sciences, University of Colorado Boulder, Boulder, Colorado*
[b] *NOAA/Earth System Research Laboratory, Boulder, Colorado*
[c] *Department of Meteorology, Naval Postgraduate School, Monterey, California*
[d] *Department of Atmospheric and Oceanic Sciences, University of California, Los Angeles, Los Angeles, California*
[e] *Physical Sciences Laboratory, NOAA/Earth System Research Laboratory, Boulder, Colorado*

(Manuscript received 25 September 2021, in final form 10 February 2022)

ABSTRACT: This study examines thermodynamic–convection coupling in observations and reanalyses, and attempts to establish process-level benchmarks needed to guide model development. Thermodynamic profiles obtained from the NOAA Integrated Global Radiosonde Archive, COSMIC-1 GPS radio occultations, and several reanalyses are examined alongside Tropical Rainfall Measuring Mission precipitation estimates. Cyclical increases and decreases in a bulk measure of lower-tropospheric convective instability are shown to be coupled to the cyclical amplification and decay of convection. This cyclical flow emerges from conditional-mean analysis in a thermodynamic space composed of two components: a measure of "undiluted" instability, which neglects lower-free-tropospheric (LFT) entrainment, and a measure of the reduction of instability by LFT entrainment. The observational and reanalysis products examined share the following qualitatively robust characterization of these convective cycles: increases in undiluted instability tend to occur when the LFT is less saturated, are followed by increases in LFT saturation and precipitation rate, which are then followed by decreases in undiluted instability. Shallow, convective, and stratiform precipitation are coupled to these cycles in a manner consistent with meteorological expectations. In situ and satellite observations differ systematically from reanalyses in their depictions of lower-tropospheric temperature and moisture variations throughout these convective cycles. When using reanalysis thermodynamic fields, these systematic differences cause variations in lower-free-tropospheric saturation deficit to appear less influential in determining the strength of convection than is suggested by observations. Disagreements among reanalyses, as well as between reanalyses and observations, pose significant challenges to process-level assessments of thermodynamic–convection coupling.

KEYWORDS: Clouds; Convective clouds; Madden-Julian oscillation; Precipitation; Convective storms; Cumulus clouds; Thermodynamics

1. Introduction

Tropical convection influences the global distribution of precipitation, brokers radiative transfer, and redistributes heat, moisture, and momentum, fundamentally shaping Earth's weather and climate. Even relatively short (~2-day) pulses of tropical convective heating have been shown to induce long-lived responses in the midlatitudes (Branstator 2014), and large-scale phenomena such as the Madden–Julian oscillation (MJO) serve as important sources of predictability on subseasonal-to-seasonal (S2S) time scales (Bjerknes 1966; Hoskins and Karoly 1981; Sardeshmukh and Hoskins 1988; Zhang 2005; Dias and Kiladis 2019; Jiang et al. 2020; Dias et al. 2021). On monthly time scales, variations in the spatial organization of tropical convection have been shown to substantially influence the global radiation balance (Bony et al. 2020). Given these global impacts, it is difficult to overstate the importance of understanding and representing the processes driving tropical convective variability (Bony et al. 2015; Stevens et al. 2019).

Thermodynamic–convection coupling plays a crucial role in determining the distribution, evolution, and organization of convection, and arises from a myriad of complex interactions spanning an enormous range of scales, as illustrated schematically in Fig. 1 (Neelin and Held 1987; Raymond 2000; Mapes et al. 2006; Khouider and Majda 2008; Kiladis et al. 2009; Adames and Ming 2018). Understanding and assessing thermodynamic–convection coupling can be aided by conceptually separating the coupling process into two distinct steps, posed here as questions that can be assessed individually:

1) How does convection respond to its thermodynamic environment?
2) How does convection, in turn, cause its thermodynamic environment to evolve?

Because thermodynamic–convection coupling is an interactive process, evolving as characteristics of the cloud population change, a third question must also be addressed:

3) How does the coevolution of convection and its thermodynamic environment change as characteristics of the cloud population change?

Given typical model development goals, this study focuses on interactions between ensembles of convection and their large-scale environment, not on those between individual convective elements and their immediate environment.

Corresponding author: Brandon Wolding, brandon.wolding@noaa.gov

DOI: 10.1175/JAS-D-21-0256.1

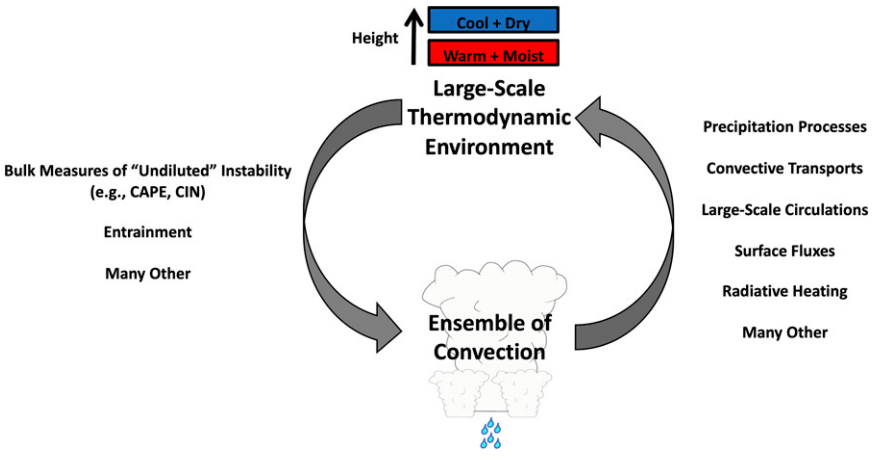

FIG. 1. Schematic illustrating the simplified conceptual approach adopted by this study, whereby thermodynamic–convection coupling is separated into two distinct steps (gray arrows). The role that particular processes play in coupling will change as the characteristics of the convective ensemble change.

A broad and influential hypothesis of how ensemble-averaged convection responds to the large-scale thermodynamic environment was put forth in convective quasi-equilibrium (QE) theory (Arakawa and Schubert 1974). A simplified and generalized definition of QE is a state of near-zero buoyancy maintained by an approximate balance between the slow production of buoyancy by large-scale forcings (e.g., surface fluxes, radiative cooling, large-scale convergence) and the fast consumption of buoyancy by convection (Arakawa 2004; Neelin et al. 2008). In this simplified QE interpretation, both the slow drive toward instability by large-scale forcings and the rapid consumption of buoyancy by convection push the atmosphere toward a "critical point" of convective instability, sometimes called the QE point, where the transition from a nonconvecting atmosphere to a convecting atmosphere occurs. Different variants of QE place varying emphasis on the importance of temperature and/or moisture fluctuations within the boundary layer and/or free troposphere for convective variability (Arakawa and Schubert 1974; Emanuel 1993; Emanuel et al. 1994; Raymond 1995; Mapes 2000; Khouider and Majda 2006; Kuang 2008; Khouider and Majda 2008; Neelin et al. 2008; Raymond and Herman 2011; Raymond et al. 2015; Raymond and Fuchs-Stone 2021). In simplified QE interpretations, ensemble-averaged convection is sometimes viewed as being "slaved to the large-scale" (Neelin et al. 2008).

Convection, in turn, has both direct and indirect impacts on the thermodynamic environment. While the direct impacts of convection are generally to reduce convective instability by vertically transporting heat and removing column water vapor, convection can also indirectly impact the thermodynamic environment through the changes that it induces in the so-called large-scale "forcing" terms. These indirect impacts can give rise to positive thermodynamic–convection feedbacks, which have been shown to contribute to large-scale convective variability such as the Madden–Julian oscillation and convective self-aggregation in idealized models (Bretherton et al. 2005; Wing and Emanuel 2014; Chikira 2014; Arnold and Randall 2015; Adames and Kim 2016). As ensemble-averaged convection not only responds to, but is also a driver of the large-scale "forcings," it has considerably more agency in determining its own variability and evolution than is immediately apparent in the simplified QE interpretation presented above.

This two-way dialogue between convection and its thermodynamic environment has been shown to give rise to the cyclical amplification and decay of convection across a broad range of spatiotemporal scales (Mapes and Houze 1993; Chen and Houze 1997; Mapes et al. 2006; Kiladis et al. 2009; Inoue and Back 2017; Wolding et al. 2020a; Inoue et al. 2021). Model intercomparison and process-level studies indicate that poor representation of the thermodynamic–convection coupling processes driving these convective cycles contributes to deficiencies in model representation of tropical convective variability (Thayer-Calder and Randall 2009; Jiang et al. 2015; Ahn et al. 2017; Rushley et al. 2018). The primary scientific goals of this study are to use process-oriented diagnostics (PODs) of thermodynamic–convective coupling to address the three questions posed above and, if possible, to establish process-level benchmarks to guide model development.

Data used in this study are described in section 2. In section 3, a bulk measure of moisture and temperature stratification in the lower troposphere is introduced, and assumptions made during its formulation and application are discussed. Section 4 introduces recently developed PODs, which are used to examine thermodynamic–convection coupling in several reanalysis products. Thermodynamic–convection coupling is examined using observations in section 5. Discussion and conclusions are provided in sections 6 and 7, respectively. Additional analyses of thermodynamic–convection coupling are provided in the appendixes.

TABLE 1. Summary of data used for each analysis in this study, and their corresponding figure numbers.

Data	Horizontal resolution	Temporal sampling	Geographical location	Years	Figure(s)
			Thermodynamic profiles		
ERAi	2.5° × 2.5°	Daily	15°N–15°S, 60°E–180°; ocean	1998–2015	Figs. 3–7
ERA5	0.25° × 0.25°	Hourly	Six warm pool IGRA stations	1998–2015	Figs. 12–14
ERA5	2.5° × 2.5°	Daily	15°N–15°S, 60°E–180°; ocean	1998–2015	Fig. 7
JRA-55	2.5° × 2.5°	Daily	15°N–15°S, 60°E–180°; ocean	1998–2015	Fig. 7
NOAA IGRA	—	Twice daily	Six warm pool IGRA stations	1970–2018	Figs. 8, 10, 12–14
COSMIC-1	Variable	Variable	15°N-15°S, 60°E–180°; ocean	2007–12	Fig. 9
Guam (PGUA)	—	Variable	13°N, 145°E	1999–2001, 2014–19	Fig. 11
			Precipitation data		
TRMM 3B42	0.5° × 0.5°	3 hourly	Six warm pool IGRA stations	1998–2015	Fig. 8
TRMM 3B42	0.5° × 0.5°	3 hourly	"Nearest" COSMIC sounding	2007–12	Fig. 9
TRMM 3B42	2.5° × 2.5°	Daily	15°N–15°S, 60°E–180°; ocean	1998–2015	Figs. 3, 4, 7
TRMM 2A23	2.5° × 2.5°	Daily	15°N–15°S, 60°E–180°; ocean	1998–2014	Figs. 5, 6
Guam (PGUA)	~2.5°	Within ±1.5 h of sounding	13°N, 145°E	1999–2001, 2014–19	Fig. 11

2. Data

Analyses are limited to the tropical Indian and west Pacific Oceans (15°N–15°S, 60°E–180°), regions that have extended sounding records and that are characterized by similar thermodynamic–convection coupling processes (Inoue et al. 2021). The geographical variability of thermodynamic–convection coupling is discussed in section 6 and appendix D. Table 1 summarizes the data used for each analysis in this study, and indicates their corresponding figure numbers.

Pressure-level fields of specific humidity q and temperature T, as well as surface pressure P_s, are obtained from ERA5, ERA-Interim (hereafter ERAi), and JRA-55 (Dee et al. 2011; Kobayashi et al. 2015; Hersbach et al. 2020). Unless otherwise noted, these data are on a 2.5° × 2.5° horizontal grid and averaged to daily temporal resolution. We also make use of two different Tropical Rainfall Measuring Mission (TRMM) precipitation data products: daily TRMM 2A23 spanning 1998–2014 is gridded at 2.5°× 2.5° resolution, and TRMM 3B42 version 7A spanning 1998–2015 at various spatiotemporal resolutions (Huffman et al. 2007). TRMM 2A23 has been modified by the procedure outlined in Funk et al. (2013), and the precipitation type classifications are detailed in subsequent sections. Additional descriptions and analyses of these data are provided by Ahmed and Schumacher (2015, 2017).

NOAA Integrated Global Radiosonde Archive (IGRA) soundings provide high-vertical-resolution, quality-controlled observations of temperature, relative humidity, dewpoint depression, wind direction, and wind speed at stations spanning the tropics (Durre et al. 2006, 2018). Additionally, IGRA provides sounding-derived moisture and stability parameters for each suitable sounding. In this study, we retrieve specific humidity from dewpoint depression, which is successfully reported more frequently than relative humidity. Each sounding is linearly interpolated in the vertical to 25-hPa resolution between the minimum and maximum reported pressure levels. Above 100 hPa, the interpolation resolution changes to include only the 70-, 50-, 30-, 20-, and 10-hPa levels. A 25-hPa threshold for the maximum distance between a reported pressure level and interpolated level has been applied. If there are no reported pressure level data within ±25 hPa of the desired interpolation level, no interpolation is performed. To minimize the potential impacts of land surface processes, analysis is limited to 0000 and 1200 UTC soundings from six "small" island stations in the tropical western Pacific Ocean (Fig. 2), defined as stations whose nearest corresponding 0.25°× 0.25° ERA5 grid point has a land fraction less than 10% (Ahmed and Schumacher 2015; Bergemann and Jakob 2016; Schiro and Neelin 2019). These six stations have exceptionally long, continuous, and high-quality sounding records, and together account for the vast majority of available small-tropical-island IGRA soundings having requisite boundary layer temperature and moisture observations. The ~115 000 soundings examined in this study span the period 1970–2018.

Constellation Observing System for Meteorology, Ionosphere and Climate (COSMIC-1) level 2 WetPrf radio occultation (RO) profiles provide high-vertical-resolution (~200 m in the lower troposphere) observations of temperature and vapor pressure, from which specific humidity is calculated. Given the limited abilities of microwave and infrared satellite sounders to measure water vapor in the presence of convection, COSMIC RO profiles are uniquely well suited for examining thermodynamic–convection coupling over

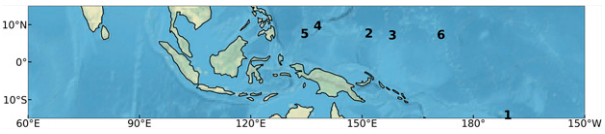

FIG. 2. Boldface numbers indicate the locations of the six NOAA IGRA sounding stations analyzed, whose corresponding station IDs are AQM00091765, FMM00091334, FMM00091348, FMM00091413, PSM00091408, and RMM00091376, respectively.

sparsely observed tropical oceans because of their global coverage and insensitivity to clouds and precipitation (Kursinski et al. 1997; Basha and Ratnam 2009; Xie et al. 2012; Pincus et al. 2017; Ho et al. 2020). Analyses are limited to quality-controlled oceanic profiles ("badness" flag = 0) with at least three observations below 850 hPa, resulting in ~83 000 RO profiles spanning 2007–12. These RO profiles typically span ~1° of latitude–longitude in the lowest 4.5 km of the troposphere, with some profiles spanning in excess of 3° of latitude/longitude, and therefore reflect relatively large-scale conditions when compared to IGRA soundings. In subsequent analyses, the average latitude and longitude values in the lowest 4.5 km are assigned to each profile.

Ground-based WSR-88D data at Guam (PGUA) provide additional estimates of rainfall from 1999 to 2001 and 2014 to 2019, and were accessed via the "noaa-nexrad-level2" S3 bucket hosted by Amazon Web Services. Rawinsondes launched at Guam provided temperature and humidity profiles (https://ruc.noaa.gov/raobs/) and were used to calculate terms in Eq. (1). The radar reflectivity factor was regridded to a rectilinear grid with spacing of 1 km and 500-m vertical spacing. The Powell et al. (2016) rain-type classification algorithm was then applied to the interpolated reflectivity at 2-km height. Based on the size of echo objects and the horizontal heterogeneity of the local reflectivity field, the algorithm classified echoes as 1) stratiform: laterally expansive regions of light rainfall; 2) convective: locally intense rainfall; 3) mixed: echoes that may contain both convective and stratiform characteristics and immediately surround a convective echo; 4) isolated convective core: convective regions of usually shallow convection; and 5) isolated convective fringe: echo containing only small hydrometeors in area immediately surrounding an isolated convective core. Rain rates were estimated using the Z–R relationships derived for convective, stratiform, and all rainfall by Thompson et al. (2018); the category for all rainfall was applied to both isolated convective fringe and mixed echo. Mean radar-derived rain rates averaged within 1.5 h of a rawinsonde launch were paired with corresponding rawinsonde-derived quantities. Any radar data collected more than 1.5 h before or after a launch were discarded. As a result, 4076 paired observations were generated.

3. Formulation of lower-tropospheric plume buoyancy

To be both insightful and widely utilized, PODs must strike a fine balance between completeness and simplicity, including sufficient complexity to capture the fundamental processes of interest, while simultaneously remaining easy to calculate using commonly available model output. In this spirit of reductionism, we have chosen to use lower-tropospheric plume buoyancy (B_L), which has been developed and examined observationally and analytically over a series of papers in recent years, as a simplified measure of the bulk thermodynamic properties of the lower troposphere (Ahmed and Neelin 2018, hereafter AN18; Ahmed et al. 2020, hereafter AAN20; Adames et al. 2021). Use of B_L attempts to reduce the complexities of vertical structure to a single measure of temperature and moisture stratification between two bulk layers, a "deep" boundary layer (DBL) stretching from the surface to 850 hPa, and a lower free troposphere (LFT) spanning from 850 to 600 hPa.

This choice of layers is motivated by the trimodal nature of tropical convection, a characteristic highlighted by the seminal observational analyses of the GATE and TOGA-COARE field campaigns, as well as subsequent radar analyses of the tropical west Pacific (Thompson et al. 1979; Johnson et al. 1999; Hollars et al. 2004). Tropical convective plumes or thermals face two primary challenges as they develop and attempt to rise through the lower troposphere: a stable layer at the trade inversion, and a second weaker stable layer near the freezing level, which on average lies at around 575 hPa over the tropical oceans (Johnson et al. 1999). If convection maintains buoyancy through the freezing level, two factors begin to support its further development and transition to deep convection; a decrease in lapse rates above the freezing level, and a "reinvigoration" from the latent heat of freezing (Johnson et al. 1999; Zipser 2003; Sahany et al. 2012; Raymond and Fuchs-Stone 2021). Therefore B_L focuses on thermodynamic factors impacting the buoyancy of convective plumes as they attempt to rise from the trade inversion to the freezing level, namely, temperature and moisture fluctuations within two layers whose variability and physical processes offer a natural distinction (Raymond et al. 2003; Tulich and Mapes 2010; Kuang 2010; Fuchs-Stone et al. 2020). Previous results have shown B_L to be an effective predictor for the onset of tropical precipitation, which increases approximately linearly as B_L increases beyond some critical threshold, making it well suited for both analytical and observational investigations of thermodynamic–convective coupling (AN18; AAN20; Adames et al. 2021).

As AN18, AAN20, and Adames et al. (2021) provide detailed derivations of B_L, we instead begin with Eq. (7) of AAN20, and focus our discussion on the process-level assumptions made during the development and application of B_L that prove particularly relevant to this study. The expression of B_L adopted by AAN20 is

$$B_L = g\left(\underbrace{w_B\frac{\tilde{\pi}e_B - e_L^*}{e_L^*}}_{\text{Term 1}} - \underbrace{w_L\frac{L_v\left(q_L^* - q_L\right)}{e_L^*}}_{\text{Term 2}}\right), \tag{1}$$

where the moist enthalpy (ME) e and $\tilde{\pi}$ are given by

$$e = C_pT + L_vq, \tag{2}$$

$$\tilde{\pi} = \left(\frac{p_L}{p_B}\right)^{R_d/C_p}, \tag{3}$$

and g is acceleration due to gravity, L_v is the latent heat of vaporization, q is specific humidity, T is temperature, and * indicates saturation values of a quantity. Subscripts B and L denote mass-weighted averages over the DBL and LFT, which span from the surface to 850 hPa and from 850 to 600 hPa, respectively, in this study. p_B = 925 hPa and

p_L = 725 hPa are the midpoint DBL and LFT pressures, respectively. Note that B_L can similarly be formulated using other quasi-conserved variables such as moist static energy (MSE) or θ_e.

The w_B and w_L parameters scale the relative influence of the DBL and LFT on plume buoyancy at the freezing level, and are given by

$$w_B = \frac{a\Delta p_B}{b\Delta p_L} \ln\left(\frac{a\Delta p_B + b\Delta p_L}{a\Delta p_B}\right), \tag{4}$$

$$w_L = 1 - w_B, \tag{5}$$

where Δp_B and Δp_L are the pressure thicknesses of the DBL and LFT, respectively. The a and b parameters are the slopes of the assumed plume mass flux profile (i.e., the rate of increase of updraft mass flux with height) within the DBL and LFT, respectively, and reflect the rates at which environmental air is entrained into the plume as it rises through these layers. AN18 "reverse-engineered" the values of a and b by applying an iterative precipitation-buoyancy curve fitting procedure to ERAi thermodynamic fields and TRMM 3B42 precipitation. In other words, by examining how convective transition statistics were impacted by small variations in assumed layer weightings, AN18 were able to identify convective mass-flux profiles (i.e., values of a and b) that yielded a nearly universal onset of observed precipitation across the tropics. The resultant profiles indicated a nearly identical linear increase in convective mass flux with height, which would imply a constant rate of entrainment throughout the DBL and LFT, such that $a \approx b$. With $a = b$, the layer weightings w_B and w_L become 0.59 and 0.41, respectively.

In treating the a and b parameters as constants, one assumes that the slope of the updraft mass flux profile below the freezing level is, to first order, independent of changes in the composition of the cloud ensemble, organizational feedbacks, and other factors. This assumption has some observational support. Examining radar wind profiler (RWP) retrievals of vertical velocity from the GoAmazon2014/15 field campaign, Schiro et al. (2018) found that both mesoscale and smaller-scale convection exhibited similar nearly linearly increasing updraft mass flux profiles throughout the depth of the lower troposphere, often referred to as "deep-inflow" mixing (Kingsmill and Houze 1999; Mechem et al. 2002; McGee and Van den Heever 2014; Martin et al. 2016). Comparing data from the GoAmazon2014/15 field campaign and Nauru Island in the tropical western Pacific, Schiro and Neelin (2019) showed that parcel buoyancy estimates based on deep-inflow mixing profiles were able to capture deep convective onset at both a tropical land and a tropical ocean site, irrespective of season or time of day, for both mesoscale and smaller-scale convection.

Term 1 in Eq. (1) has previously been characterized as a measure of "undiluted" lower-tropospheric instability that neglects the impacts of LFT entrainment on plume buoyancy (AN18; AAN20; Adames et al. 2021). Term 2 is a measure of the "dilution" of buoyancy that a rising plume experiences due to LFT entrainment of subsaturated environmental air (Bretherton et al. 2004; Peters and Neelin 2006; Holloway and Neelin 2009; Neelin et al. 2009; Ahmed and Schumacher 2017). Previous characterizations of term 1 are not entirely correct, as a plume that is nonentraining in the LFT will be defined by a $w_B = 1$. "Undiluted B_L" is therefore more correctly defined by

$$\text{Undiluted } B_L = U = g\left(\frac{\tilde{\pi}e_B - e_L^*}{e_L^*}\right). \tag{6}$$

Using this new definition of undiluted B_L, we can rewrite B_L as

$$B_L = U \underbrace{- (U - B_L)}_{\text{Dilution of } B_L}, \tag{7}$$

which can again be rewritten as

$$B_L = g\left(\underbrace{\frac{\tilde{\pi}e_B - e_L^*}{e_L^*}}_{\text{Undiluted } B_L} \underbrace{- w_L \frac{\tilde{\pi}e_B - e_L^*}{e_L^*} - w_L \frac{e_L^* - e_L}{e_L^*}}_{\text{Dilution of } B_L}\right). \tag{8}$$

Equation (8) is equivalent to Eq. (1), and indicates that "dilution of B_L" results from LFT entrainment of subsaturated environmental air, as well as LFT entrainment of environmental air whose temperature differs from that of the plume. These terms are highly anticorrelated, and neither is negligible (not shown). While the sum of these entrainment impacts on plume buoyancy have the potential of being either positive or negative, and would therefore be better described as "modification" of B_L, we retain the "dilution" terminology for consistency with previous work. In words, Eq. (8) describes a bulk measure of convective instability meant to mimic the buoyancy a theoretical plume experiences while rising through the LFT. It assumes that the plume was launched from 1000 hPa and has already undergone deep-inflow mixing in the DBL. The decomposition of B_L into "undiluted" and "dilution" components are therefore related specifically to entrainment occurring in the LFT.

4. Thermodynamic–convection coupling in reanalyses

As B_L was originally "reverse-engineered" by AN18 using ERAi thermodynamic fields and TRMM precipitation, we will begin our examination of thermodynamic–convection coupling using these data. To provide context for subsequent results, we will first examine a conventional B_L–precipitation curve. Figure 3 shows TRMM 3B42 precipitation rate (solid black line, left Y axis) as a function of ERAi B_L for the time period of 1998–2015, where data have been limited to the tropical Indian and west Pacific Oceans (15°N–15°S, 60°E–180°). Precipitation is effectively suppressed at very negative values of B_L, and increases rapidly as B_L increases beyond some "critical point" ($B_{L,\text{crit}}$), where the phase transition from a non-deep-convecting atmosphere ($B_L < B_{L,\text{crit}}$) to a deep-convecting atmosphere ($B_L > B_{L,\text{crit}}$) occurs. In this study, the mode (gray dashed vertical line) of the PDF of B_L (black dashed line, right Y axis) is used to objectively approximate the value of $B_{L,\text{crit}}$ (Neelin et al. 2008). A simplified and generalized QE interpretation (black schematic arrows) would suggest that the broad PDF to the left of the critical point results from large-scale forcings slowly driving the atmosphere toward instability, and that

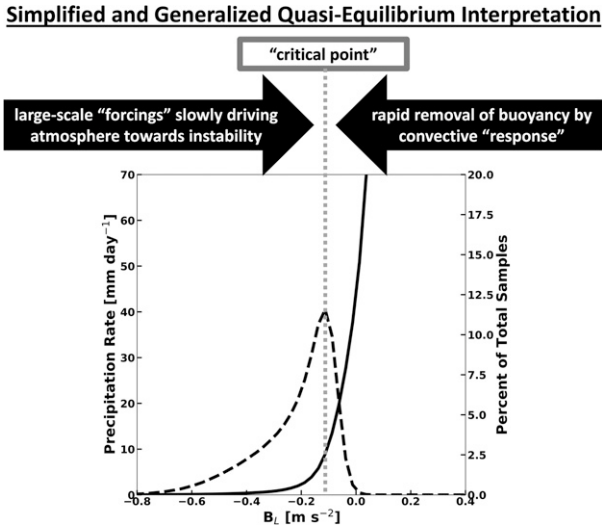

FIG. 3. Bin-mean daily average 2.5° TRMM 3B42 precipitation rate (solid black line, left Y axis) as a function of ERAi B_L, where data were separated into bins of B_L of width 0.025 m s^{-2}. The PDF of B_L (dashed black line, right Y axis) is given as the percentage of total samples, with the mode (i.e., bin with largest number of samples) indicated by the vertical dashed gray line. Black schematic arrows suggest processes that, from a simplified quasi-equilibrium perspective, drive the atmosphere toward the "critical point" ($B_{L,\mathrm{crit}}$) or QE point, where the phase transition from a nonconvecting atmosphere ($B_L < B_{L,\mathrm{crit}}$) to a convecting atmosphere ($B_L > B_{L,\mathrm{crit}}$) occurs.

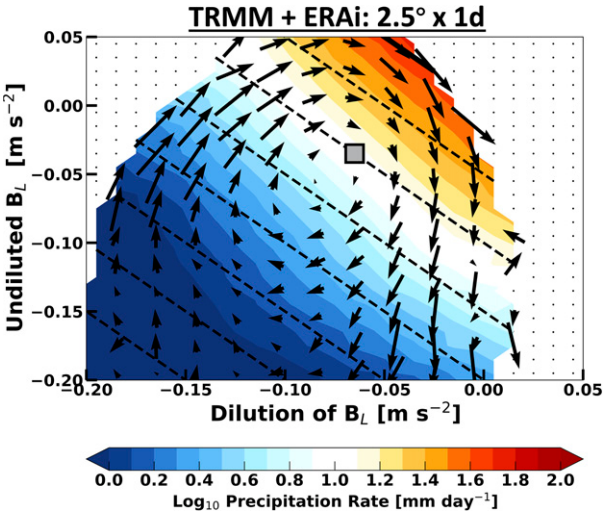

FIG. 4. Data were separated into bins of width 0.01 m s^{-2} along the X and Y axes. Color shading shows bin-mean TRMM precipitation rate (log scale). Vectors indicate the temporal coevolution of the system, calculated as the bin-mean temporal centered differences of undiluted B_L and dilution of B_L using daily data. Vector centers are plotted at bin centers, and have been scaled by a factor of 2 to aid visualization. The gray square marks the mode (i.e., the bin with the most samples). Black contours show total B_L contoured in intervals of 0.05 m s^{-2}, with B_L = 0 m s^{-2} contoured as a thick solid line, negative values contoured as thin dashed lines, and positive values contoured as thin solid lines when present. Stippling denotes bins containing less than 200 samples, which are not plotted.

the rapid drop off of the PDF to the right of the critical point results from the rapid removal of buoyancy by convection. Both the slow drive toward instability by large-scale forcings and the rapid removal of buoyancy by convection push the atmosphere toward the critical point, where the coupled system spends most of its time (i.e., approximately the mode of the PDF).

Broadening the analysis of the B_L–precipitation curve to consider the individual components of B_L, as well as their temporal coevolution, offers an opportunity to reexamine this interpretation of QE, and reassess the relative importance of moisture and temperature fluctuations in driving convection (Wolding et al. 2020a). In Fig. 4, data were first separated into bins of undiluted B_L (Y axis) and dilution of B_L (X axis) of width 0.01 m s^{-2}. Color shading shows the bin mean TRMM precipitation rate (log scale). Vectors indicate the temporal coevolution of the system, calculated as the bin-mean temporal centered differences of undiluted B_L and dilution of B_L using daily data. Vector centers are plotted at bin centers, and have been scaled by a factor of 2 to aid visualization. The gray square marks the mode (i.e., the bin with the most samples), and the number of samples within each bin declines approximately logarithmically with distance from the mode, such that regions near the periphery of B_L space are sampled much less frequently than regions closer to the mode (appendix A, Fig. A1). Black contours show total B_L in intervals of 0.05 m s^{-2}, increasing toward the upper-right corner of the figure. The B_L = 0 m s^{-2} is contoured in a thick solid line, and negative values are contoured in thin dashed lines. Stippling denotes bins containing less than 200 samples, which are not plotted.

Precipitation is effectively suppressed at very negative values of B_L (lower-left corner), and increases rapidly as B_L increases beyond the mode (gray square) which, in a QE interpretation, sits on or near the "critical line" or QE line (i.e., a line of constant $B_L = B_{L,\mathrm{crit}}$). The tendency for color shaded precipitation rate to roughly align with the contours of total B_L in Fig. 4 suggests that precipitation rate is not impacted by changes in the relative contributions of undiluted B_L and dilution of B_L to the total buoyancy. In other words, a large-scale environment with relatively high undiluted B_L and a relatively large dilution of B_L (e.g., dry LFT) appears to produce roughly the same amount of precipitation as an environment with relatively low undiluted B_L and a relatively small dilution of B_L (e.g., moist LFT), as long as the total B_L of the two environments is similar.

Vectors, which indicate the temporal coevolution of undiluted B_L and dilution of B_L, trace a clear clockwise evolution around the mode: i.e., undiluted B_L preferentially increases when the LFT is less saturated, LFT saturation preferentially increases when undiluted B_L is positive, and undiluted B_L preferentially decreases when LFT conditions are closer to saturation. This suggests that the system preferentially evolves in a cyclical manner. Recall that vectors are calculated using bin-mean temporal centered differences, which are the sum of the temporal backward (hereafter leading) and forward (hereafter

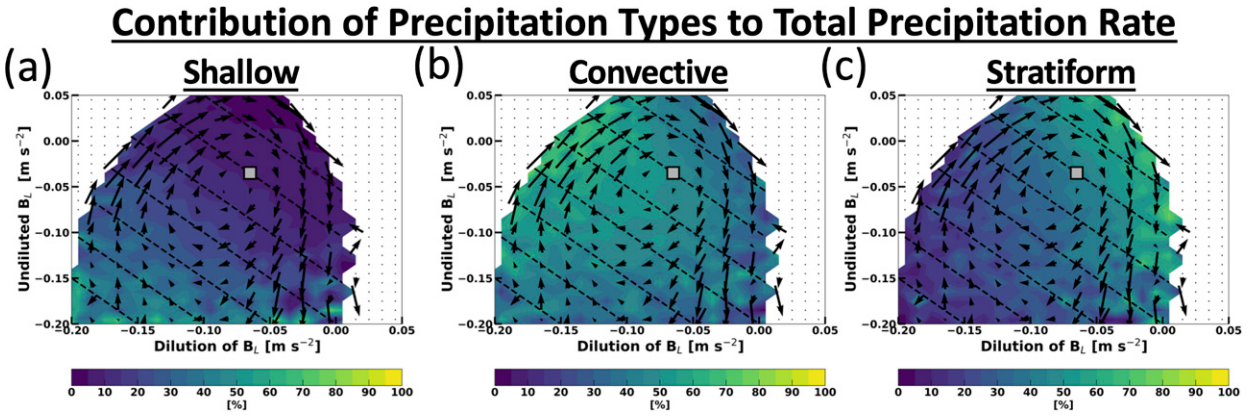

FIG. 5. As in Fig. 4, except color shading shows TRMM 2A23 estimates of the contribution of (a) shallow, (b) convective, and (c) stratiform precipitation types to the total precipitation rate (i.e., Fig. 4, color shading). Note that TRMM 2A23 precipitation spans 1998–2014, while vectors are calculated using ERAi thermodynamic fields from 1998 to 2015, as in Fig. 4.

lagging) differences. The leading and lagging behavior of the system is to move away from and back toward the mode, respectively, with the mode acting as an attractor of the system [detailed in appendix B and Wolding et al. (2020a)]. The mode therefore appears to be a special preferred state on the QE line (for the mean large-scale forcing), referred to here as a QE point, the "destination of the adjustment responding to the large-scale forcing" (Arakawa 2004). The clockwise evolution seen in Fig. 4 therefore represents the small residual of these forcings away from and adjustments back toward the QE point, which do not exactly cancel. This cyclical net evolution only arises from the aggregated effect of numerous buoyancy perturbations (see appendix B; Inoue and Back 2017; Wolding et al. 2020a; Inoue et al. 2021).

We wish to examine what role the changing characteristics of the cloud ensemble may play in driving the cyclical evolution of the coupled system. Figure 5 shows how the relative contributions of shallow, convective, and stratiform TRMM precipitation types to the total TRMM precipitation rate (i.e., Fig. 4, color shading) vary with changes in undiluted B_L and dilution of B_L. These precipitation type classifications reflect the primary mechanisms of hydrometeor growth, which occurs primarily through collision–coalescence and/or riming in the shallow and convective types (Funk et al. 2013). While both shallow and convective precipitation types can be generated by "convective" processes, the shallow classification indicates precipitation generated exclusively below the freezing level. The stratiform type refers to precipitation whose growth occurs primarily via vapor deposition above the freezing level, as often occurs in stratiform anvils associated with deep convection. Precipitation produced by low-level stratiform clouds (e.g., regions of large-scale subsidence) would be considered "shallow" under this classification system. These precipitation type definitions were motivated by the impacts that vertical heating structure has on large-scale circulations, the top-heaviness of large-scale vertical velocity, and attendant energy transports, which can contribute to thermodynamic–convection coupling feedbacks (Houze 1982; Hartmann et al. 1984; Schumacher et al. 2004; Back and Bretherton 2006; Zhang and Hagos 2009; Raymond et al. 2009; Wolding and Maloney 2015; Wolding et al. 2016; Inoue and Back 2017; Inoue et al. 2020, 2021).

Examination of the lower-left corner of Fig. 5 indicates that shallow precipitation is the primary precipitation type occurring in very stable environments ($B_L \ll B_{L,\mathrm{crit}}$). Moving clockwise around the periphery of B_L space indicates that as the environment becomes more unstable ($B_L \approx B_{L,\mathrm{crit}}$) and precipitation rates begin to increase rapidly (Fig. 4, color shading), the predominant precipitation type transitions from shallow to convective. During this shallow to convective transition, vectors point upward and to the right, suggesting that the net effect of the cloud ensemble is to further destabilize the environment (i.e., increase B_L). When the environment becomes highly unstable and precipitation rates reach their peak (Fig. 4, upper-right corner), with undiluted B_L achieving its most positive values and the LFT approaching saturation, the predominant precipitation type transitions from convective to stratiform (Fig. 5c). Examination of rain area and conditional rain rates (not shown) suggests that these high precipitation rates result from a dramatic expansion in the areal coverage of the stratiform precipitation type. At this stage vectors begin to point downward, indicating that the net effect of the cloud ensemble is to reduce undiluted B_L and stabilize the environment. The results of Schiro et al. (2020, their Fig. 7), who examined thermodynamic–precipitation pickup curves for non-MCS and MCS precipitation separately, suggest that the increased contribution of stratiform precipitation near and below $B_{L,\mathrm{crit}}$ is indicative of MCSs contributing a larger fraction of the total precipitation rate. Vectors then begin to point left as the environment stabilizes and precipitation rate decreases (i.e., B_L decreasing below $B_{L,\mathrm{crit}}$), suggesting a drying of the LFT.

Taken together, Figs. 4 and 5 suggest that precipitation rate varies primarily as a function of B_L, and is relatively insensitive to changes in the composition of the cloud ensemble, and changes in the relative contributions of undiluted B_L and dilution of B_L. These results suggest that AN18 identified appropriate layer weightings (w_B and w_L) using their "reverse-

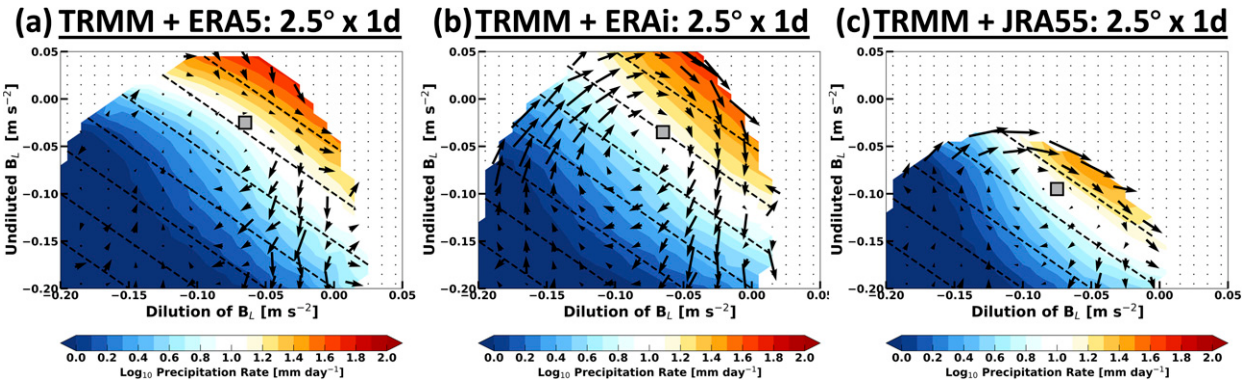

FIG. 6. As in Fig. 4, but for (a) ERA5 thermodynamic fields, (b) ERAi thermodynamic fields, and (c) JRA-55 thermodynamic fields. TRMM precipitation was used in all cases. Note that (b) is the same as Fig. 4, recreated here to facilitate comparison.

engineering" methodology, and support the "deep-inflow" assumptions made during the development and application of B_L.

As the cyclical amplification and decay of convection is coupled to cyclical increases and decreases in B_L, the processes controlling the temporal evolution of B_L are of utmost interest. A relatively straightforward methodological approach to such a problem would be to use budget analyses to examine the primary balances and/or imbalances of processes that give rise to the temporal evolution of moisture and temperature within the DBL and LFT (i.e., the vectors in Fig. 4; e.g., Adames et al. 2021). However, there may be a problem with this approach. Before embarking on such a budget analysis, it is prudent to ensure that reasonable agreement in the depiction of thermodynamic–convection coupling exists among different reanalysis products.

Figure 6 provides such a comparison, where TRMM 3B42 precipitation has been used in concert with thermodynamic fields from ERA5, ERAi, and JRA-55 datasets for the time period of 1998–2015. The three reanalyses agree on the most general characteristics of thermodynamic–convection coupling, namely, that precipitation rate increases with increasing B_L, and that the thermodynamic environment evolves in a clockwise fashion around the mode in B_L space. Yet the three reanalyses disagree to a considerable extent about several characteristics of thermodynamic–convection coupling, including the value of $B_{L,\text{crit}}$, the rate at which precipitation increases as B_L increases beyond $B_{L,\text{crit}}$, the maximum values of B_L obtained, and the degree to which buoyancy perturbations away from the QE point drive a net evolution of the coupled system. As the same TRMM 3B42 precipitation product has been used in each analysis, this indicates that reanalyses do not agree on how moisture and/or temperature within the DBL and/or LFT evolve in relation to observed precipitation. These disagreements among reanalyses become more pronounced when reanalysis precipitation is used in place of TRMM 3B42 precipitation for this analysis (see appendix C).

5. Thermodynamic–convection coupling in observations

In light of the considerable disagreement among reanalyses documented in the previous section, in situ and satellite observations will now be used to assess how reanalyses compare to more direct measurements of moisture and temperature. Comparing thermodynamic profiles from NOAA IGRA soundings to those from reanalyses is complicated by both the presence of land at the IGRA stations, as well as the differing spatiotemporal resolution of the data (e.g., point measurement vs area average). Previous studies have shown that land surface processes such as strong diurnal heating and land–sea-breeze organization can alter thermodynamic–-precipitation relationships (Ahmed and Schumacher 2015; Bergemann and Jakob 2016; Schiro and Neelin 2019). Point measurements such as soundings may be impacted by localized precipitation that modifies boundary layer thermodynamic conditions at small scales, and may not be representative of the thermodynamic conditions impacting precipitation measured on larger scales. Furthermore, while many characteristics of convective cycles exhibit considerable spatiotemporal-scale invariance, the rate of increase in precipitation with increasing B_L (i.e., the precipitation "pickup") has been shown to be impacted by spatiotemporal averaging and stochastic fluctuations (Peters and Neelin 2006; Neelin et al. 2009; AAN20; Wolding et al. 2020a; Inoue et al. 2021). Discussion in this section is therefore focused on results that appear robust across analyses of different observational products and varying spatiotemporal scales. Additionally, a comparison of the ERAi and NOAA IGRA analyses at different spatiotemporal scales is provided in appendix D.

With the aforementioned uncertainties and caveats in mind, consider Fig. 7, which shows the analysis of NOAA IGRA soundings from six small-tropical-island stations in the western Pacific that have especially long, continuous, and high-quality sounding records. IGRA thermodynamic profiles have been matched with the "nearest" (in space and time) 0.5° 3-h-resolution TRMM 3B42 precipitation data, which span the shorter period of 1998–2015. IGRA soundings show the temporal coevolution of the system (vectors) tracing a clockwise pattern around the mode in B_L space, similar to the pattern seen in reanalyses (Fig. 6), though more elliptical with undiluted B_L as the major axis. Importantly, the IGRA analysis shows a notably different relationship between precipitation rate (color shading) and the thermodynamic environment than

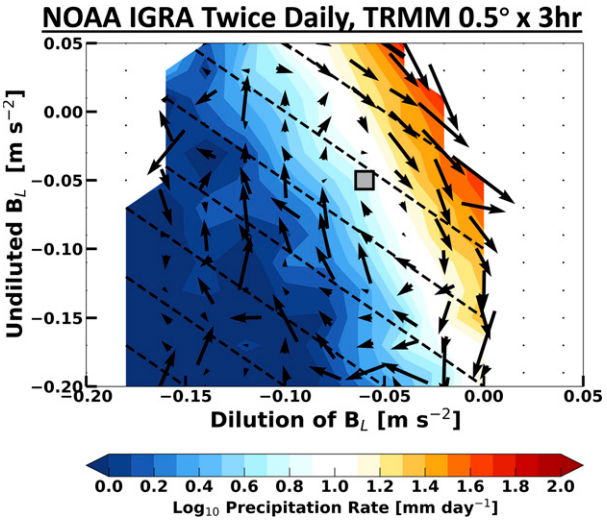

FIG. 7. As in Fig. 4, but for thermodynamic fields obtained from twice-daily soundings spanning 1970–2018 at six small-tropical-island stations in the western Pacific. IGRA soundings were matched with the "nearest" (in space and time) 0.5° 3-h-resolution TRMM 3B42 precipitation data, which span the shorter period of 1998–2015. A minimum of 200 samples per bin was used for plotting vectors and, due to the shorter precipitation record, a lesser threshold of 100 samples per bin was used for color shading. Stippling denotes bins containing less than the required number of samples, which are not plotted. Data were separated into bins of width 0.02 m s^{-2} along the X and Y axes.

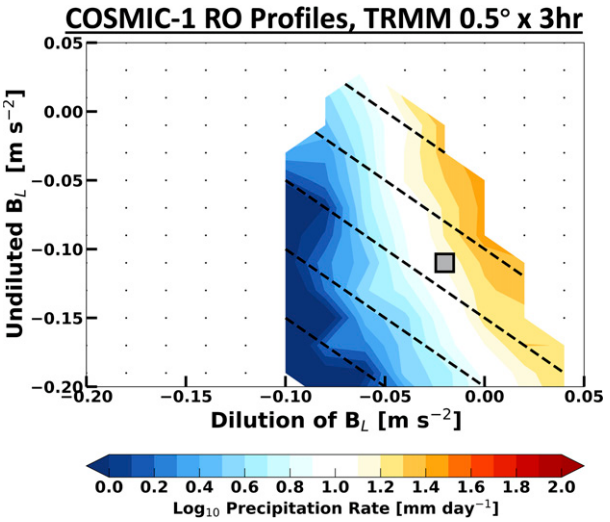

FIG. 8. As in Fig. 4, but for thermodynamic fields obtained from COSMIC-1 radio occultation (RO) profiles spanning 2007–12. RO thermodynamic fields were matched with the "nearest" (in space and time) 0.5° 3-h-resolution TRMM 3B42 precipitation data. Stippling denotes bins containing less than 200 samples, which are not plotted. Data were separated into bins of width 0.02 m s^{-2} along the X and Y axes.

was seen in reanalyses, with precipitation rate showing much less sensitivity to variations in undiluted B_L in the IGRA analysis, and much more sensitivity to variations in dilution of B_L.

In an effort to verify that the thermodynamic–precipitation relationship seen in Fig. 7 is not adversely impacted by the presence of the islands, nor by the point-measurement nature of soundings, we repeated the analysis using tropical oceanic COSMIC-1 RO thermodynamic profiles. RO profiles are limb occultations that typically span a degree or more of latitude and/or longitude in the lower troposphere, and therefore reflect relatively large-scale conditions when compared to the IGRA soundings. COSMIC-1 thermodynamic profiles were collocated with the "nearest" (in space and time) 0.5° 3-h-resolution TRMM 3B42 precipitation data, shown in Fig. 8. Given the irregular spatiotemporal sampling of RO profiles, the temporal coevolution of the system (i.e., vectors) could not be calculated in this analysis. While the precipitation pickup is more gradual than in the IGRA analysis (Fig. 7), likely due to the coarse horizontal resolution of the RO profiles, the results confirm that precipitation rate shows more sensitivity to variations in dilution of B_L than was suggested by reanalyses, as indicated by the more negatively sloped lines of constant precipitation rate (color shading) in B_L space (Fig. 8). One potential physical interpretation of the higher sensitivity of precipitation rate to variations in dilution of B_L is that convective mass flux may increase more rapidly with height in the LFT than it does in the DBL [i.e., $b > a$ in Eq. (4)].

Select IGRA sounding-derived quantities exhibiting coherent variations within B_L space are shown in Fig. 9. Again tracing a clockwise pattern around the mode, maximum values of bin-mean CAPE (Fig. 9b) occur just prior to the rapid increase in precipitation rates (Fig. 9a). As precipitation rates approach their maximum values, CAPE decreases rapidly, CIN begins to increase (Fig. 9c), and bin-mean 850–500-hPa wind shear begins to increase (Fig. 9d). The evolution of 1000–850- and 1000–500-hPa wind shear (not shown) is very similar to that seen in Fig. 9d. Figures 9e and 9f, which show the standard deviation of 950-hPa wind speed and temperature within each bin in B_L space, respectively, indicate that near-surface wind speed variance and near-surface temperature variance are also increasing at these times. This may be indicative of increased "triggering energy" (e.g., cold pools) (Mapes 2000), which may help convection to overcome the relative dearth of low-level buoyancy and increased convective inhibition seen at these times. Additionally, convective downdrafts that reduce DBL ME and increase CIN can also increase DBL ME variance, such that regions of high ME may remain despite decreased area mean ME (Nicholls and Lemone 1980; Kingsmill and Houze 1999; Mapes 2000). As precipitation rates decrease, bin-mean CIN becomes even more negative, and wind shear, near-surface wind speed variance, and near-surface temperature variance remain elevated.

Given the limited overlap of IGRA soundings and TRMM 2A23 precipitation data, rawinsonde data and radar retrievals collocated in Guam are used to provide a precipitation type analysis that does not depend on reanalysis thermodynamic fields. This analysis provides a "bottom-up" perspective that compliments the top-down perspective of the previous analysis (Fig. 5), and implements the precipitation classification algorithm of Powell et al. (2016), which includes an additional

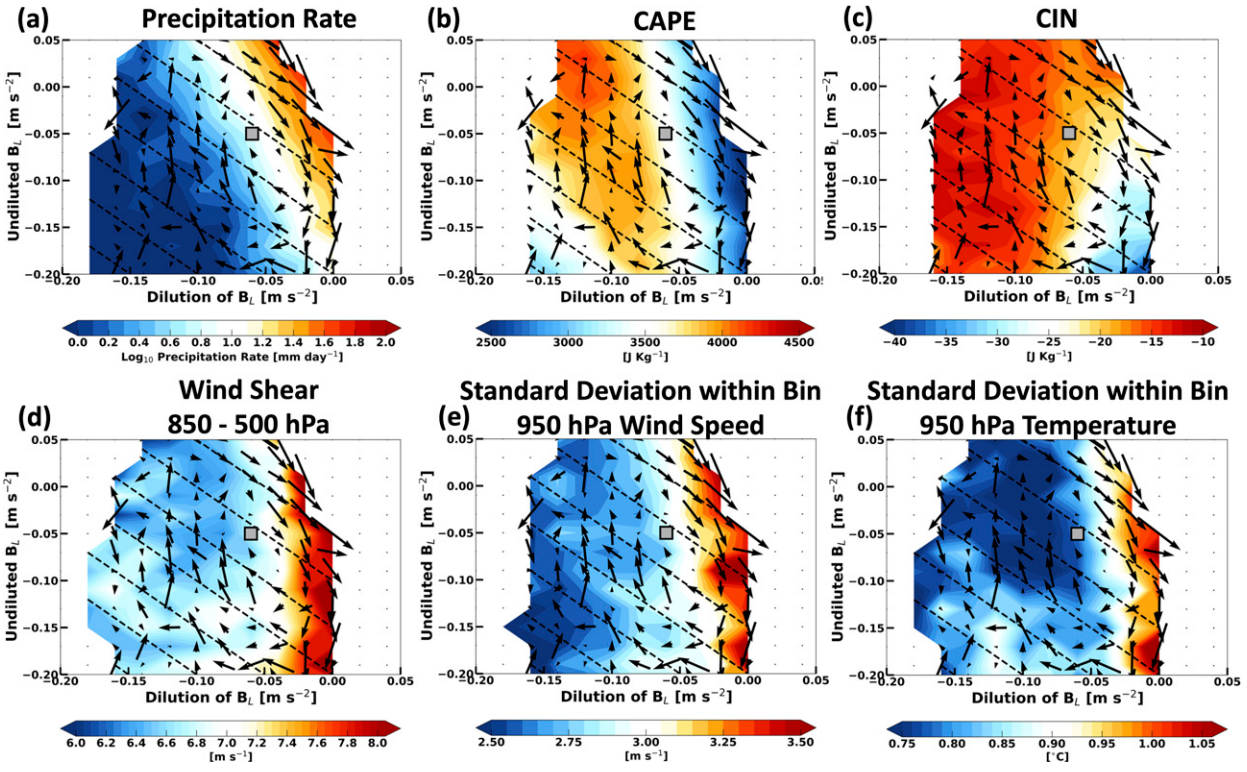

FIG. 9. (a) As in Fig. 7, recreated here to facilitate comparison. (b)–(f) As in Fig. 7, except color shading indicates IGRA sounding-derived (b) bin-mean CAPE, (c) bin-mean CIN, (d) bin-mean 850–500-hPa wind shear, (e) bin standard deviation of 950-hPa wind speed, and (f) bin standard deviation of 950-hPa temperature. Stippling denotes bins containing less than 200 samples, which are not plotted.

precipitation type for precipitation exhibiting "mixed" convective and stratiform characteristics. Detailed comparisons of these analyses are complicated by their differing precipitation type classifications, as well as the relatively limited data available at Guam. Therefore, the Guam analysis is presented solely to emphasize that coherent changes in the characteristics of the cloud ensemble occur throughout B_L space, and are not artifacts of the TRMM 2A23 precipitation analysis. Figure 10 shows how the relative contributions of isolated, convective, and mixed and stratiform precipitation types to the total precipitation rate vary with changes in undiluted B_L and dilution of B_L. Moving clockwise around the mode (gray square) indicates that the predominant precipitation type changes from isolated, to convective, to mixed and stratiform, a progression characteristic of a prototypical convective life cycle (Mapes and Houze 1993; Chen and Houze 1997; Mapes et al. 2006; Kiladis et al. 2009; Inoue and Back 2017).

That the IGRA sounding analysis and the RO analysis agree on the main features of the dependence of precipitation rate on B_L lends strong support to the notion that the observational

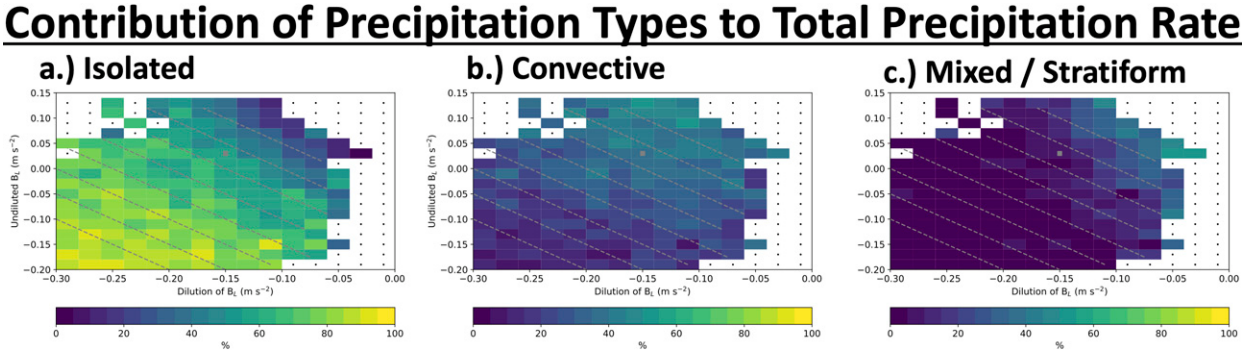

FIG. 10. As in Fig. 5, but for the percentage of rain attributed to (a) isolated convective core and fringe combined, (b) convective, and (c) mixed and stratiform precipitation types, derived using Guam WSR-88D data and nearby rawinsonde data as described in section 2. Vectors are omitted because of small sample size.

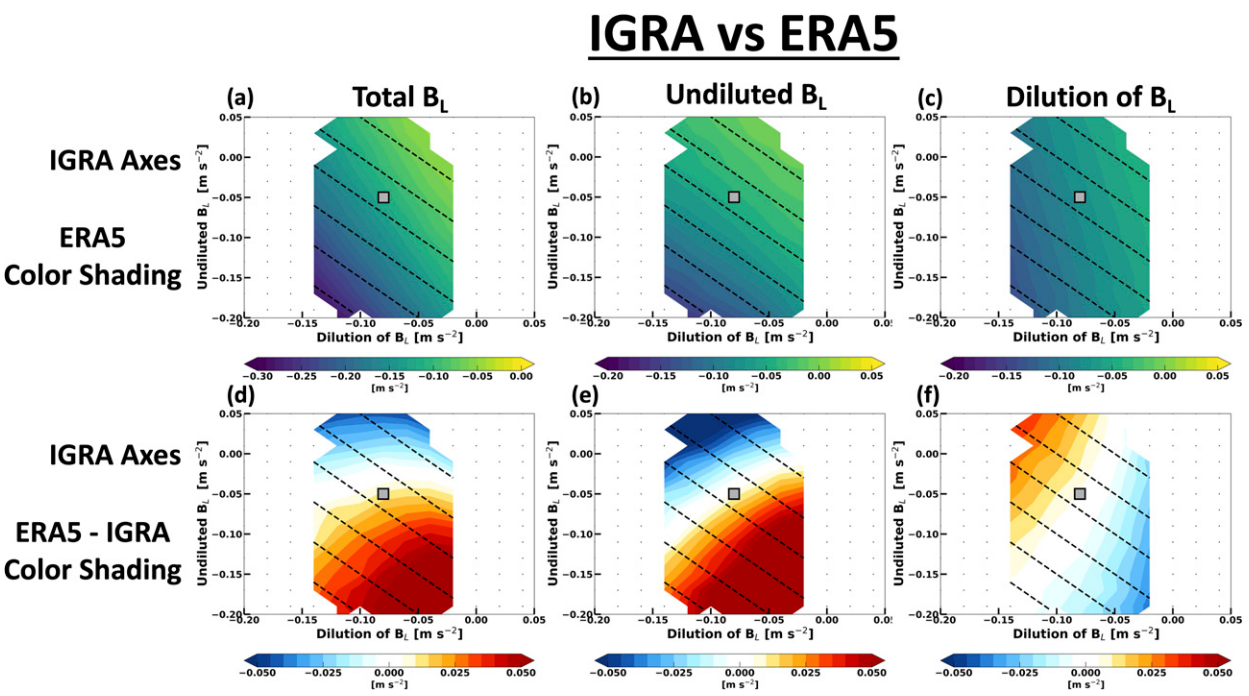

FIG. 11. ERA5 data spanning 1998–2015 were separated into bins of width 0.02 m s^{-2} according to their corresponding IGRA profile values of dilution of B_L and undiluted B_L (X and Y axes, respectively). Color shading shows bin-mean (a) ERA5 B_L, (b) ERA5 undiluted B_L, (c) ERA5 dilution of B_L. (d)–(f) The difference between ERA5 and IGRA for each of these terms. The gray square marks the mode of IGRA data (i.e., the bin with the most samples). Black contours show total B_L from IGRA contoured in intervals of 0.05 m s^{-2}, with B_L = 0 m s^{-2} contoured as a thick solid line, and negative values contoured as thin dashed lines. Stippling denotes bins containing less than 200 samples, which are not plotted.

results of Figs. 7 and 8 are a better representation of reality than the reanalysis results of Fig. 6. The discrepancies between reanalyses and observations will now be examined in further detail.

Discrepancies between thermodynamic–convection coupling in observations and reanalyses

To further examine the discrepancies between how observations and reanalyses characterize thermodynamic–convection coupling, IGRA thermodynamic profiles spanning 1998–2015 were matched with the "nearest" 0.25° hourly ERA5 thermodynamic profiles, and the values of B_L, undiluted B_L, and dilution of B_L were computed for each set of profiles. ERA5 data were then separated into bins of width 0.02 m s^{-2} according to their corresponding IGRA profile values of undiluted B_L and dilution of B_L.

In the top row of Fig. 11, color shading shows how the bin mean values of (Fig. 11a) ERA5 B_L, (Fig. 11b) ERA5 undiluted B_L, and (Fig. 11c) ERA5 dilution of B_L vary as a function of IGRA dilution of B_L (X axis) and IGRA undiluted B_L (Y axis). The bottom row of Fig. 11 shows the difference of ERA5 minus IGRA (i.e., the disagreement) for each of these terms in color shading, where IGRA data have again been used for the X and Y axes. Disagreements between ERA5 B_L and IGRA B_L (Fig. 11d) arise primarily from disagreements in undiluted B_L (Fig. 11e), with disagreements in dilution of B_L (Fig. 11f) being relatively small. Figure 11e suggests that ERA5 generally underestimates the magnitude of both large positive and large negative values of undiluted B_L (i.e., underestimates the extremes), but does so in a way that shifts or tilts the values of ERA5 undiluted B_L by roughly 45° clockwise in B_L space relative to their IGRA counterparts (Fig. 11b). The net effect of these systematic differences in undiluted B_L and dilution of B_L is that lines of constant ERA5 B_L are shifted roughly 25° clockwise in B_L space relative to their IGRA counterparts (Fig. 11a), which in turn gives rise to the "phase shift" in the relationship between B_L and precipitation that is seen when comparing reanalyses (Fig. 6) and observations (Fig. 7).

To further examine the vertical structure of differences between IGRA and reanalysis thermodynamic profiles, we define a buoyancy perturbation index (BPI) which can be used to classify and composite data based on its thermodynamic state. The magnitude and phase of the BPI are given by

$$\text{magnitude} = \left(\text{Undiluted } B_L'^2 + \text{Dilution of } B_L'^2\right)^{1/2}, \tag{9}$$

$$\text{phase} = \tan^{-1}\left(\frac{\text{Undiluted } B_L'}{\text{Dilution of } B_L'}\right), \tag{10}$$

where prime indicates a buoyancy perturbation from its value at the QE point, objectively defined as the mode (Figs. 7 and 11, gray square). The magnitude of the BPI quantifies the

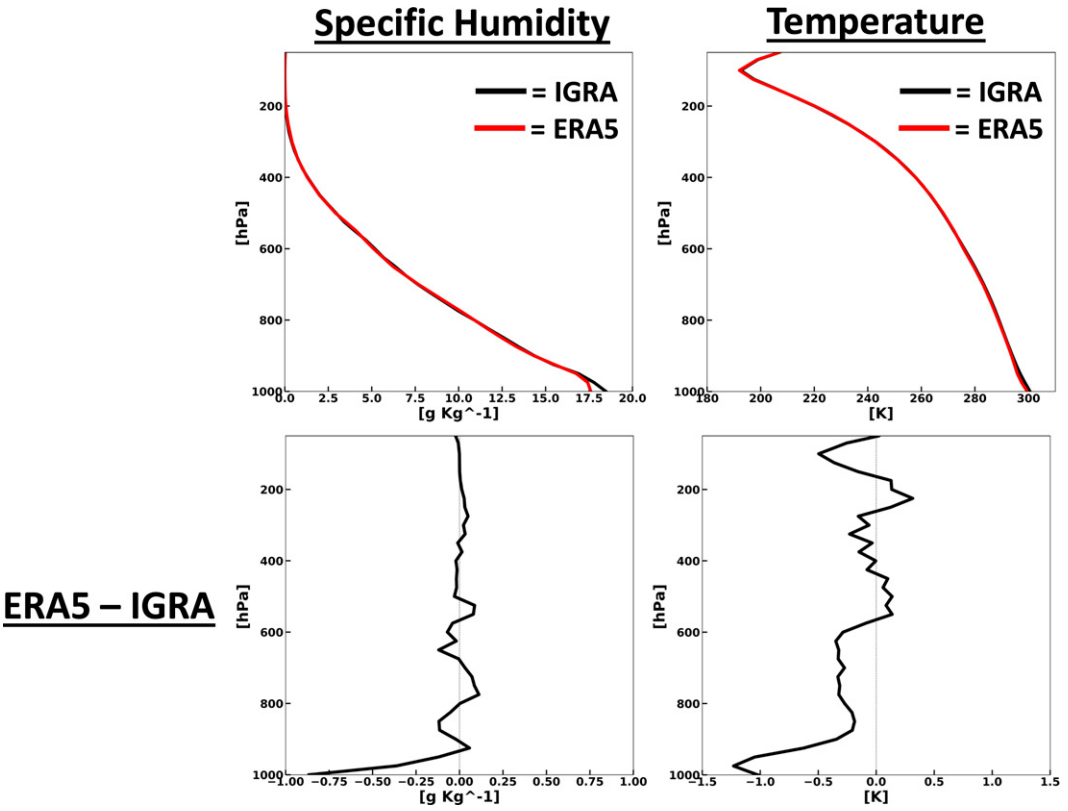

FIG. 12. (top) Composite IGRA (black) and ERA5 (red) thermodynamic profiles, and (bottom) differences between ERA5 and IGRA profiles, for the IGRA QE point (i.e., very close to the mode in Figs. 7 and 11). Data were limited to those whose corresponding IGRA buoyancy perturbation index (BPI) magnitude is less than 0.01 m s^{-2} for the time period of 1998 to 2015. This resulted in 1706 profiles, which were then averaged together.

magnitude of the buoyancy perturbation away from the QE point, and has units of m s^{-2}. The phase of the BPI is determined by the relative contributions of undiluted B_L and dilution of B_L to the buoyancy perturbation, and has values spanning ±180°. A phase of 180° corresponds to a negative perturbation in dilution of B_L, a phase of 90° corresponds to a positive perturbation in undiluted B_L, a phase of 0° corresponds to a positive perturbation in dilution of B_L, and a phase of −90° corresponds to a negative perturbation in undiluted B_L. Thus, a BPI with constant magnitude 0.05 m s^{-2} and phase decreasing from 180° to −180° would trace a clockwise circle of radius 0.05 m s^{-2} around the mode in Figs. 7 and 11.

BPI values were calculated for each of the IGRA soundings from 1998 to 2015. To examine "QE point" thermodynamic profiles, IGRA soundings were limited to those whose corresponding BPI magnitude is less than 0.01 m s^{-2} (i.e., very close to the mode in Figs. 7 and 11). For each of the remaining IGRA soundings, the "nearest" 0.25° hourly ERA5 thermodynamic profile was selected, and composites of both sets of profiles were made. Figure 12 shows composite QE point profiles of specific humidity and temperature for IGRA (black line) and ERA5 (red line). Unsurprisingly these profiles are similar to tropical profiles commonly observed during lightly precipitating conditions (e.g., Fig. 1 in Holloway and Neelin (2009). The differences between IGRA and ERA5 profiles (bottom row) of specific humidity are small, but ERA5 temperature exhibits a cold bias in the DBL and LFT relative to IGRA.

The vertical structure of buoyancy perturbations away from these QE point profiles were examined by limiting IGRA soundings to those whose corresponding BPI magnitude is between 0.025 and 0.05 m s^{-2}, which corresponds to a moderate buoyancy perturbation. The remaining IGRA soundings were then separated into bins of width 15° spanning ±180° based on their corresponding BPI phase. Again, for each of the IGRA soundings in each phase bin, the "nearest" 0.25° hourly ERA5 thermodynamic profile was selected, and composites of both sets of profiles were made. Figure 13 shows the composite buoyancy perturbation profiles of specific humidity and temperature for IGRA (top row) and ERA5 (middle row). To emphasize the structure of specific humidity and temperature variations, the respective IGRA and ERA5 QE point profiles have been subtracted. The bottom panel shows the difference between ERA5 and IGRA profiles, where the QE point profile bias has been included. Moisture and temperature variations above the freezing level (~575 hPa) are fairly well represented in

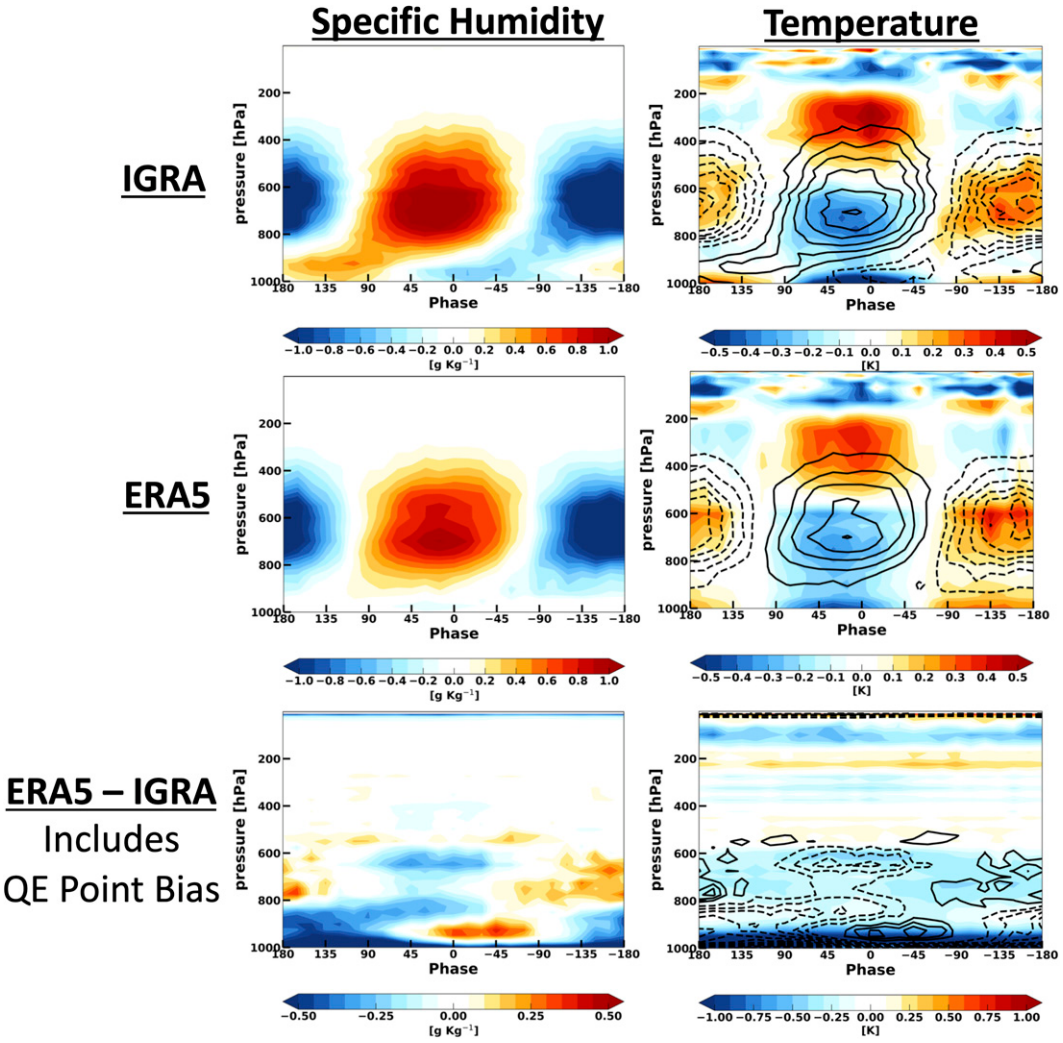

FIG. 13. Vertical structure of buoyancy perturbations away from composite QE point profiles (Fig. 12, top) for (top) IGRA and (middle) ERA5. (bottom) Differences between ERA5 and IGRA, which includes QE point biases (Fig. 12, bottom). (right) Specific humidity perturbations are contoured every 0.2 g Kg^{-1} in the top and middle rows, and every 0.1 g Kg^{-1} in the bottom row, with positive values in solid contours, and negative values in dashed contours. Moving from left to right along the X axis shows IGRA BPI phase decreasing from 180° to −180°, which is analogous to tracing a clockwise circle of radius 0.025–0.05 m s^{-2} around the mode in Figs. 7 and 11. A phase of 180° corresponds to a negative perturbation in dilution of B_L, a phase of 90° corresponds to a positive perturbation in undiluted B_L, a phase of 0° corresponds to a positive perturbation in dilution of B_L, and a phase of −90° corresponds to a negative perturbation in undiluted B_L. Data from 1998 to 2015 were limited to those whose corresponding IGRA BPI magnitude is between 0.025 and 0.05 m s^{-2}, and separated into bins of width 15° spanning ±180° based on their corresponding IGRA BPI phase. This resulted in between 493 and 1696 profiles per phase bin.

ERA5. A dipole structure of small differences in both moisture and temperature occurs near the freezing level, with ERA5 being a little colder and drier than IGRA just below the freezing level during periods of intense convection (i.e., phases of 45° to 0°). Systematic differences between IGRA and ERA5 specific humidity variations are evident in the DBL, with ERA5 underestimating the magnitude of moisture variations relative to IGRA. Systematic differences between IGRA and ERA5 specific humidity variations in the DBL are accompanied by compensating differences of the opposite sign in the LFT.

6. Discussion

a. *Potential sources of discrepancies between thermodynamic–convection coupling in observations and reanalyses*

We have shown that observations and reanalyses disagree on the timing and magnitude of moisture and temperature variations that are coupled to the cyclical amplification and decay of convection, especially variations occurring within the boundary layer. When using reanalysis thermodynamic fields,

these differences cause variations in dilution of B_L to appear less influential (relative to variations in undiluted B_L) in determining the strength of convection than is suggested by observations. This can be seen by examining the slope of the lines of constant precipitation rate (color shading) in B_L space, which are more negatively sloped in observations (Figs. 7 and 8) than in reanalyses (Figs. 6 and C1).

Despite undergoing extensive quality controls, various and varied biases in temperature and humidity have been documented in both NOAA IGRA soundings and COSMIC RO profiles (Durre et al. 2006; Ho et al. 2010; Durre et al. 2018; Ho et al. 2020). Additionally, both NOAA IGRA soundings and COSMIC RO profiles have spatiotemporal sampling characteristics that differ from reanalyses. Therefore, it is possible that the discrepancies between how observations and reanalyses characterize thermodynamic–convection coupling arise from biases within the observations themselves, or from the spatiotemporal-scale differences between observations and reanalyses.

However, the large disagreement among reanalyses clearly indicates that their representation of lower-tropospheric thermodynamic variability is poorly constrained, a finding consistent with recent reanalysis intercomparison studies (Schröder et al. 2016; Yasunaga et al. 2019; Ren et al. 2021). Additionally, NOAA IGRA soundings and COSMIC RO profiles have distinct observational limitations and differ in sampling frequency and resolution, yet still agree on the main features of the dependence of precipitation rate on B_L. Taken together, these findings suggest that discrepancies among reanalyses, as well as between reanalyses and observations, may result from the relative dearth of thermodynamic observations in the marine atmospheric boundary layer, which creates a large dependence on the assimilating model and its parameterized treatments of processes impacting moisture and temperature variability in the lower troposphere (Pincus et al. 2017).

Due to the relatively sparse availability of observations in the tropics, particularly in the atmospheric boundary layer over the open ocean where issues related to ducting and superrefraction often prevent assimilation of RO data, the vertical thermodynamic structure of reanalyses is poorly constrained and subject to systematic errors arising from parameterized processes (Poli et al. 2010; Xie et al. 2012; Pincus et al. 2017; Ho et al. 2020; Ren et al. 2021). While passive microwave and infrared measurements help to constrain total column water vapor at large scales over remote tropical oceans, the vertical distribution of water vapor can be heavily influenced by the assimilating model (Pincus et al. 2017). Pincus et al. (2017) showed that the lack of observational constraints on MABL humidity, combined with the coarse vertical resolution of infrared and microwave sounders, allows analysis systems to make compensating errors in the vertical structure of humidity that approximately preserve column integrated water vapor, which is more strongly constrained by observations. Compensating errors similar to those seen in Fig. 13 are also evident in climatological profiles of humidity over the warm pool in various reanalyses (see Ren et al. 2021, Fig. 2h).

One physical interpretation of the observed B_L–precipitation relationship is that convective mass flux increases more rapidly with height in the lower free troposphere than it does in the boundary layer [i.e., $b > a$ in Eq. (4)]. In other words, convective plumes may entrain environmental air more rapidly as they rise through the lower free troposphere than they do as they rise through the boundary layer. While the deep-inflow mixing assumptions made in the formulation of B_L benefit from limited observational support, further investigation is certainly warranted (Schiro et al. 2018). Unfortunately, there are few long-running observational datasets with which to characterize the evolution of convective mass flux and its dependence on the characteristics of the cloud ensemble, and the uniquely well-suited Darwin observational supersite was decommissioned in 2017 (Kumar et al. 2015; Schiro et al. 2018; Retsch et al. 2020). Such data limitations may challenge further observational assessment of deep-inflow mixing assumptions related to mesoscale organization, large-scale vertical velocity structure, and other processes.

b. *Convective quasi equilibrium and the cyclical amplification and decay of convection*

Convective QE theory posits that both the slow drive toward instability by large-scale "forcings" (e.g., surface fluxes, radiative cooling, large-scale convergence) and the rapid consumption of buoyancy by convection push the atmosphere toward a "critical point" of convective instability, where the transition from a non-convecting atmosphere to a convecting atmosphere occurs. The results of this study suggest that, of the various and varied thermodynamic conditions that can produce a critical quantity of convective instability, preferred thermodynamic states, referred to as QE points, arise in convecting regions of the tropics.

The composition of the cloud ensemble at a QE point appears to be unique in its ability to consume large-scale convective instability at the same rate that it is being produced by "background" large-scale forcings and its own self-induced feedbacks (e.g., convectively driven large-scale circulations). Buoyancy perturbations away from a QE point are associated with changes in the convective-to-stratiform (CS) precipitation ratio (Fig. 5), which is known to impact the vertical structure of apparent heating, the top-heaviness of large-scale vertical velocity, attendant large-scale convergence/divergence, and the efficiency with which convection imports/exports moisture and MSE from the column (Houze 1982; Schumacher et al. 2004; Back and Bretherton 2006; Raymond et al. 2009; Chikira 2014; Inoue and Back 2017; Inoue et al. 2021). Buoyancy perturbations are adjusted back toward the QE point, but result in a small net evolution of the thermodynamic environment from its preperturbation state (appendix B). Integrated over numerous buoyancy perturbations, these incremental net evolutions drive cyclical increases and decreases in large-scale convective instability around the QE point, which are coupled to the cyclical amplification and decay of convection (appendix B). Larger buoyancy perturbations are associated with larger changes in the CS ratio which may, through the aforementioned large-scale circulation feedbacks and other processes (Fig. 1), contribute to a larger net evolution of system. Inoue and Back (2017) highlight that because of these feedbacks, the current state of the coupled

system (i.e., location in B_L space) can confer valuable prognostic information regarding the subsequent amplification or decay of convection.

Inoue et al. (2021), who examined convective cycles using ERAi column-integrated MSE budgets and TRMM 3B42 precipitation, found horizontal moisture advection to be the primary driver of day-to-day precipitation variations in tropical convergence zones. Positive "column-process" feedbacks were shown to drive the spontaneous amplification of precipitation in the absence of horizontal advective drying (Chikira 2014; Wolding et al. 2016; Inoue et al. 2021). Uncertainties documented in the present study suggest that the findings of Inoue et al. (2021), while both insightful and intriguing, should be confirmed against thermodynamic budgets calculated from other reanalysis and observational datasets.

This study focused on the Indian and western Pacific Oceans (IOWP), regions which Inoue et al. (2021) found to be characterized by similar convective-coupling processes. While results of an analysis limited to the central Pacific Ocean (CP) (see appendix D, section b) appear remarkably similar to those from the IOWP in this diagnostic framework, Inoue et al. (2021) highlight that the primary balances and imbalances of processes driving convective cycles in the CP differ from those in the IOWP. Future studies should therefore take geographical variability into account when examining the processes underlying thermodynamic–convection coupling.

7. Summary and conclusions

In this study, newly developed process-oriented diagnostics (PODs) were used to examine thermodynamic–convection coupling in observations and reanalyses. The PODs are based on a reductionist measure of convective instability known as lower-tropospheric plume buoyancy (B_L), which depends on moisture and temperature stratification in the lower troposphere (AN18; AAN20; Adames et al. 2021). These PODs were applied to thermodynamic profiles obtained from the NOAA Integrated Global Radiosonde Archive, COSMIC-1 GPS radio occultations, and several reanalyses, as well as precipitation estimates from the Tropical Rainfall Measuring Mission. The application of these PODs has led us to make the following main conclusions:

1) Cyclical increases and decreases in B_L are coupled to the cyclical amplification and decay of convection.
2) In situ observations and radio occultation profiles differ systematically from reanalyses in their depictions of lower-tropospheric temperature and moisture variations throughout these convective cycles.
3) When using reanalysis thermodynamic fields, these systematic differences cause variations in lower-free-tropospheric saturation deficit to appear less influential in determining the strength of convection than is suggested by observations.

The cyclical amplification and decay of convection emerges as a conditional-mean flow in a thermodynamic space composed of two components: undiluted B_L, a measure of convective instability which neglects lower-free-tropospheric (LFT) entrainment, and dilution of B_L, a measure of the impacts of LFT entrainment on convective instability. The observational and reanalysis products examined share the following qualitatively robust characterization of these convective cycles: undiluted B_L preferentially increases when the LFT is less saturated, LFT saturation preferentially increases when undiluted B_L is positive, and undiluted B_L preferentially decreases when LFT conditions are closer to saturation. This conditional-mean flow is the residual of numerous comparatively large buoyancy fluctuations [detailed in appendix B and Wolding et al. (2020a)]. Shallow, convective, and stratiform precipitation are coupled to these cycles in a manner consistent with meteorological expectations.

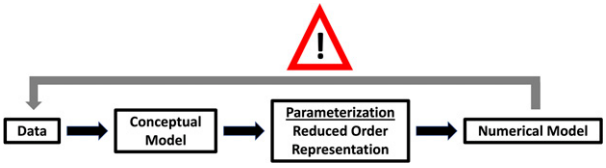

FIG. 14. Schematic illustrating common Earth system science approach to understanding and modeling complex processes and systems, and the potential hazard of self-affirmation that arises when model-influenced data are reintegrated into the workflow. Data inform simplified conceptual models of how complex processes and systems work. The simplified conceptual models guide development of reduced-order representations (i.e., parameterizations) of these complex processes and systems, which can then be incorporated into numerical models. Reintegration of numerical model output into earlier stages of this workflow, as is sometimes necessitated by the scarcity and/or structure of observational data, risks self-affirming assessments of conceptual models and parameterizations. Individuals' awareness of this potential hazard may be reduced by the penchant of Earth system scientists to work primarily within only one of the schematic boxes of this workflow.

Understanding the primary balances and imbalances of processes that give rise to cyclical increases and decreases in B_L represents an important step toward better understanding and representing convective variability in the tropics. A primary goal of this study was to use reanalyses and observations to establish process-level benchmarks of thermodynamic–convection coupling, which could then be used to guide model development. Unfortunately, this study has shown that considerable disagreement exists among reanalyses, as well as between reanalyses and observations, as to how the thermodynamic environment evolves in relation to observed convection. Such disagreement suggests that the feasibility of using thermodynamic budgets calculated from reanalyses to more fully characterize thermodynamic–convection coupling may be limited. While field campaign data (e.g., DYNAMO, OTREC) may allow more reliable calculations of such thermodynamic budgets, the relatively short length of these data may be insufficient to reduce the "noise" inherent in analyses of stochastic convection (Yoneyama et al. 2013; Sobel et al. 2014; Johnson et al. 2014; Fuchs-Stone et al. 2020). While such challenges may currently limit the establishment of clear process-level benchmarks, PODs have nonetheless proven useful for identifying process-level sources of intermodel spread in thermodynamic–convection coupling (Ahmed and Neelin 2021). Global CPM

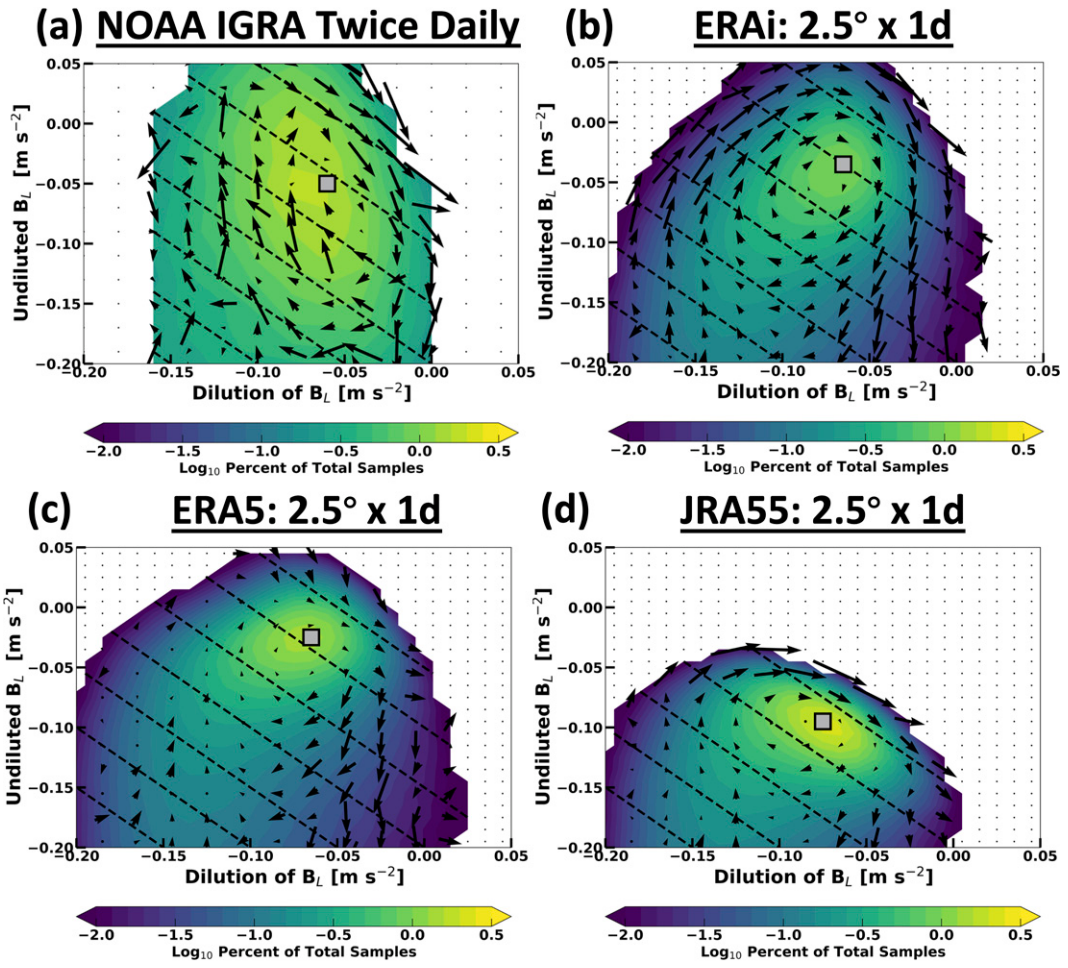

FIG. A1. As in Fig. 4, except that color shading indicates the percentage of total samples that are located within each bin (i.e., the PDF) for (a) NOAA IGRA soundings, (b) ERAi, (c) ERA5, and (d) JRA-55. Note that color shading is on a logarithmic scale. A minimum of 200 samples per bin was used for plotting vectors, and no threshold was applied for color shading. Stippling denotes completely unpopulated bins.

simulations, such as those involved in the DYAMOND project (Stevens et al. 2019), may provide fruitful avenues for future investigation of thermodynamic–convection coupling.

One potential source of the discrepancies among reanalyses, as well as between reanalyses and observations, is the lack of thermodynamic observations in the marine atmospheric boundary layer, which creates a large dependence on the assimilating model and its parameterized treatments of processes impacting moisture and temperature variability in the lower troposphere (Pincus et al. 2017). Expanded observations that can be assimilated by global forecast models will be required to better constrain tropical marine atmospheric boundary layer thermodynamic variability. Yet previous studies have highlighted that in the absence of targeted process-level model improvements, the benefits of expanded observations may go largely unexploited by reanalyses and forecasts (e.g., Pincus et al. 2017).

Reanalysis products offer the benefit of broad and continuous spatiotemporal coverage of the tropics at a resolution that can be matched to that of satellite precipitation products, making them a convenient choice for studies of thermodynamic–convection coupling. This study is a reminder of the potential hazards of allowing model-influenced data to be reintegrated into the Earth system science workflow of understanding and modeling complex processes and systems, as illustrated in Fig. 14. Previous studies of thermodynamic–convection coupling that have relied solely on reanalysis thermodynamic fields, such as Wolding et al. (2020a,b), should be interpreted with caution, and their findings reexamined in future work using more direct observations when possible. Convective mass flux variations, mesoscale convective organization, and processes impacting convective instability will be further examined in the context of thermodynamic–convection coupling in future work.

Acknowledgments. Lead author Wolding extends his gratitude to several colleagues whose contributions helped improve the analysis and discussion in this study: David Randall, Robert Pincus, Kathleen Schiro, John Peters, Walter Hannah, Yuan-Ming Cheng, Tristan L'Ecuyer, Hannah

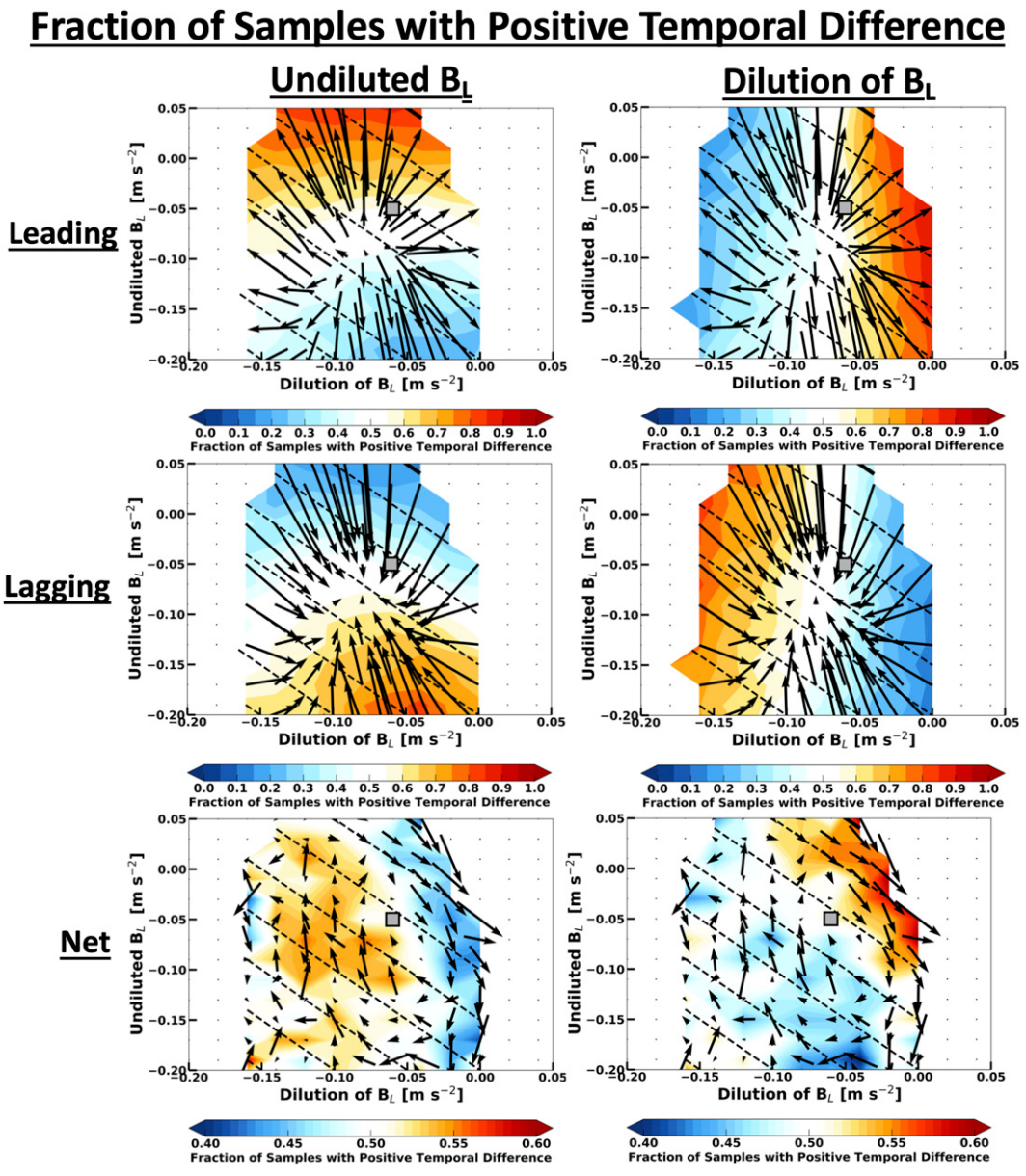

FIG. B1. As in Fig. 7, except color shading indicates the fraction of samples within each bin having a positive temporal difference of (left) undiluted B_L and (right) dilution of B_L for the time period considered.

Huelsing, Stefan Tulich, Lisa Bengtsson, and Charlotte DeMott. The authors also thank Larissa Back and two anonymous reviewers for their insightful comments and suggestions, which helped to improve this manuscript. BW was partially supported by the California Department for Water Resources (CDWR). FA and JDN were supported in part by NSF AGS-1936810 and NOAA NA21OAR4310354. SWP was supported by the Office of Naval Research under Grant N0001421WX01472.

Data availability statement. The ERA5, ERAi, JRA-55, TRMM precipitation, NOAA IGRA, and COSMIC-1 GPS RO data that support the findings of this study are publicly available from the NCAR Research Data Archive (RDA) at https://rda.ucar.edu. The radar data that support the findings of this study are available from Amazon Web Services, at https://s3.amazonaws.com/noaa-nexrad-level2/index.html. The modeling data that support the findings of this study are available from the authors upon reasonable request and with permission of associated institutions.

APPENDIX A

PDFs of IGRA Soundings and Reanalyses

Figure A1 shows PDFs of undiluted B_L and dilution of B_L, calculated using thermodynamic fields from (Fig. A1a)

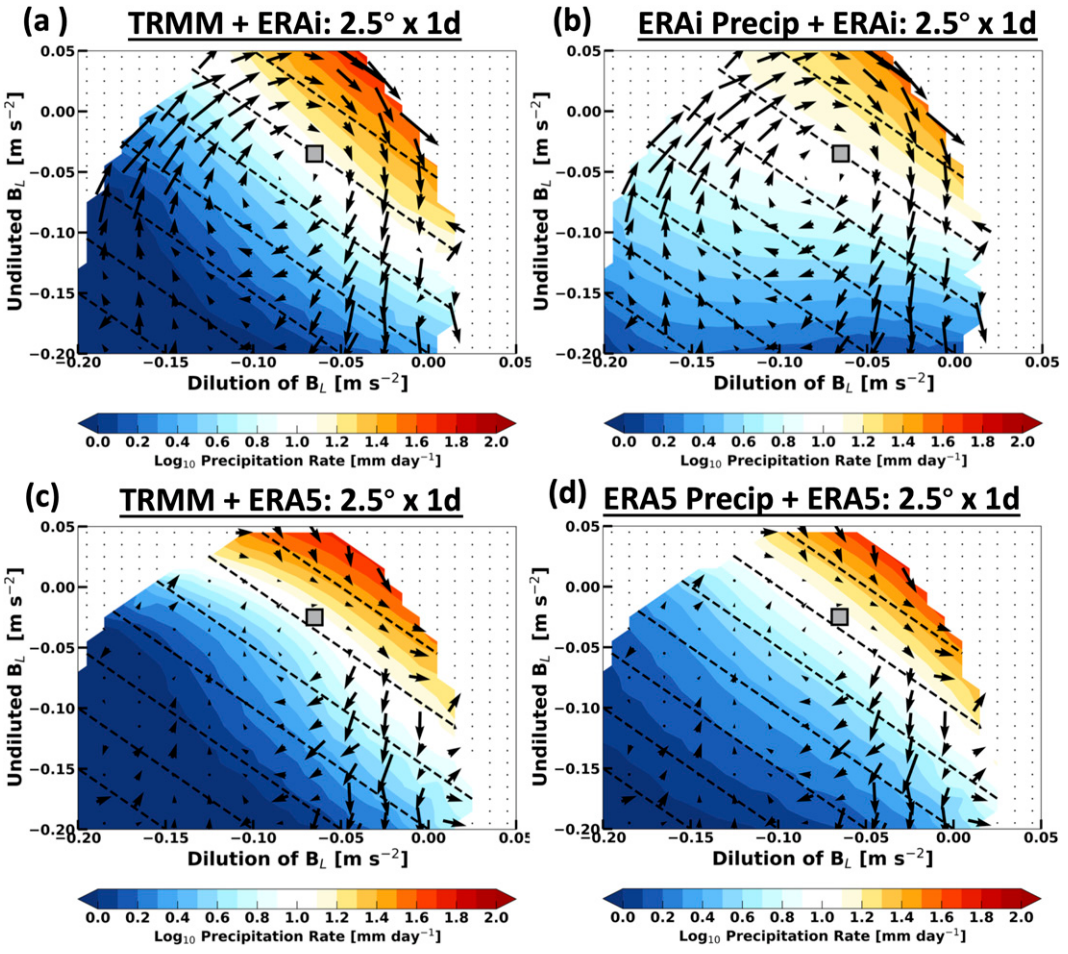

FIG. C1. (a),(c) As in Fig. 6b and Fig. 6a, respectively, repeated here to facilitate comparison. (b),(d) As in (a) and (c), except that reanalysis precipitation was used in place of TRMM 3B42 precipitation.

NOAA IGRA soundings, (Fig. A1b) ERAi, (Fig. A1c) ERA5, and (Fig. A1d) JRA-55. Samples decrease approximately logarithmically with distance from the mode in B_L space. The major axis of the elliptically shaped PDF is oriented more in line with undiluted B_L in NOAA IGRA soundings than in reanalyses.

APPENDIX B

Leading, Lagging, and Net Temporal Evolution

Figure B1 shows the leading, lagging, and net temporal coevolution of undiluted B_L and dilution of B_L for the sample of soundings used to construct Fig. 7. "Leading" shows the evolution over the 12 h leading up to the observations in each bin, calculated using bin-mean backward temporal differences. "Lagging" shows the evolution over the 12 h following the observations in each bin, calculated using bin-mean forward temporal differences. "Net" shows the evolution over the 24 h centered on the observations in each bin, which is calculated using bin-mean centered temporal differences, and represents the sum effect of the leading and lagging evolutions. The fraction of samples within each bin having a positive temporal difference of undiluted B_L (left column) and dilution of B_L (right column) is color shaded. Vectors are the same within each row of plots, where leading, lagging, and net vectors are plotted with vector heads, vector tails, and vector centers at bin centers, respectively. Please note that net vector magnitudes are scaled by a factor of 2 to aid visualization (bottom row), and that the color scale differs from those of the leading and lagging evolutions.

Vectors generally diverge away from and converge back toward the mode of the PDF (Fig. A1a) in the leading and lagging evolutions, respectively, but their offset is inexact, resulting in a net evolution of the system. The magnitude of the resulting net evolution is small relative to the leading perturbations and lagging forcings and/or adjustments from which it arises. In the net evolution (bottom row, note color bar limits), the fraction of samples in each bin having a

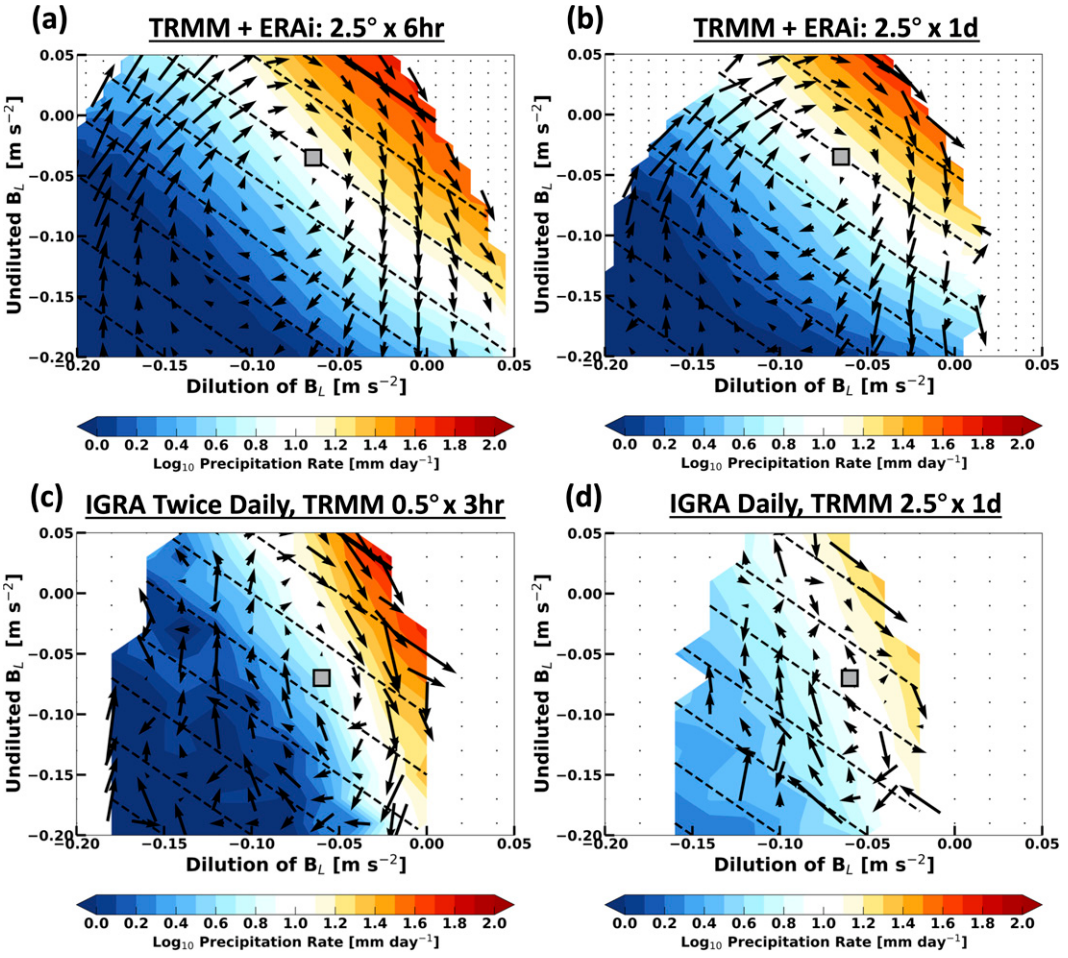

FIG. D1. (a) As in Fig. 4, except data are 6 hourly. (b) As in Fig. 4, repeated here to facilitate comparison. (c) As in Fig. 7. (d) As in Fig. 7, except twice-daily soundings were averaged to daily before calculating B_L, and TRMM 3B42 precipitation is daily averaged at 2.5°× 2.5° horizontal resolution.

positive temporal difference of undiluted B_L or dilution of B_L rarely drops below 0.4 or exceeds 0.6. This suggests that the cyclical net evolution seen in Fig. B1 only arises from the aggregated effect of numerous buoyancy perturbations. This net evolution is consistent with the orbital fluctuations in the GMS plane documented by Inoue and Back (2017). The absence of any lagging or net evolution at the QE point indicates that the precipitating cloud population (Fig. 10) is able to consume B_L at approximately the same rate at which it is being produced, and do so without changing the relative contributions of undiluted B_L and dilution of B_L.

APPENDIX C

Comparison of Thermodynamic–Convection Coupling Using Observed versus Reanalysis Precipitation

Figure C1 shows the POD applied to TRMM 3B42 precipitation (left column) and reanalysis precipitation (right column) for ERAi (top row) and ERA5 (bottom row). At precipitation rates less than 10 mm day^{-1} (cool color shading), ERAi precipitation (Fig. C1b) shows very little sensitivity to variations in dilution of B_L, similar to many CMIP5 models examined by Rushley et al. (2018). At precipitation rates greater than 10 mm day^{-1} (warm color shading), ERAi precipitation (Fig. C1b) shows a similar sensitivity to variations in undiluted B_L and dilution of B_L as is seen in TRMM precipitation (Fig. C1a), although the overall increase in precipitation rate with increasing B_L is more gradual in ERAi precipitation than in TRMM. ERA5 precipitation (Fig. C1d) has similar characteristics to TRMM precipitation (Fig. C1c), but has an earlier and more gradual increase in precipitation rate with increasing B_L than TRMM. Process studies of convection, even those leveraging thermodynamic fields from reanalysis, often elect to use observational estimates of precipitation, as reanalysis estimates of precipitation are highly dependent on parameterizations of processes such as convection.

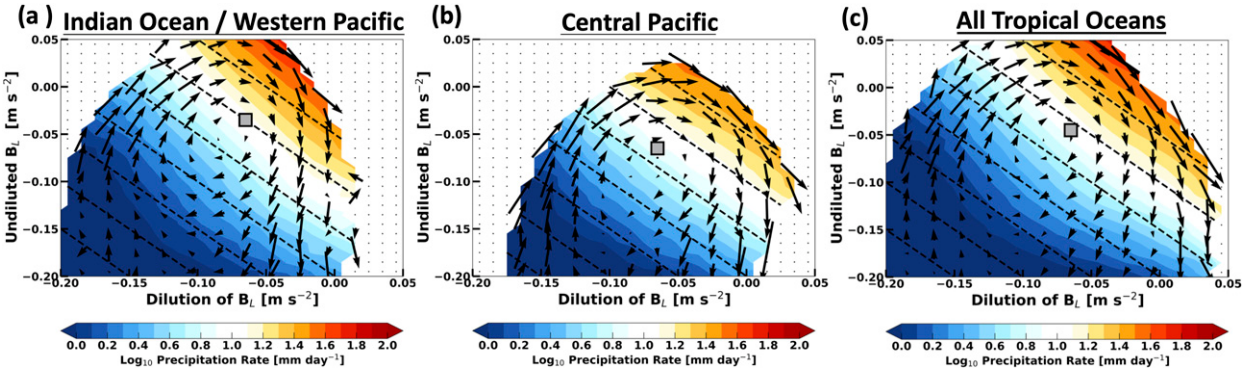

FIG. D2. (a) As in Fig. 4, where data were limited to the Indian and western Pacific Oceans (15°N–15°S, 60°E–180°), repeated here to facilitate comparison. (b),(c) As in (a), except data were limited to the central Pacific Ocean (15°N–0°, 180°–240°E) and all tropical oceans (15°N–15°S), respectively.

APPENDIX D

Spatiotemporal-Scale Dependence and Geographical Variability of Thermodynamic–Convection Coupling Analysis

a. Spatiotemporal-scale dependence

Previous studies examining thermodynamic–convection coupling have documented a considerable degree of scale invariant behavior, consistent with "slow-drive fast dissipation" systems with a critical-point attractor (Peters and Neelin 2006; Neelin et al. 2009; Inoue and Back 2017; Wolding et al. 2020a; Inoue et al. 2021). Spatiotemporal averaging has been shown to result in an earlier and more gradual increase in precipitation with increasing B_L (AAN20).

Figures D1a and D1b show the POD applied to TRMM precipitation and ERAi thermodynamic fields at 6-hourly and daily time scales, respectively, where 2.5° × 2.5° horizontal resolution has been used in both cases. The general characteristics of thermodynamic–convection coupling remain largely unchanged between the 6-hourly and daily time scales, though the latter shows an earlier and more gradual increase in precipitation rate with increasing B_L, consistent with AAN20. At daily time scales (Figs. D1b), the clockwise evolution of the vectors become less consistent toward the periphery of B_L space, likely a result of the smaller sample size of the daily data. Figures D1c and D1d show the POD applied to TRMM precipitation and IGRA thermodynamic fields across a broader range of spatiotemporal scales. Again, the larger-spatiotemporal-scale data show an earlier and more gradual increase in precipitation rate with increasing B_L. Note that the negative slope of lines of constant precipitation rate (color shading) in B_L space is not impacted by averaging of the IGRA and TRMM data to larger spatiotemporal scales (Figs. D1c,d).

b. Geographical variability

Figures D2a, D2b, and D2c show the POD applied to data limited to the IOWP (15°N–15°S, 60°E–180°), central Pacific Ocean (CP; 15°N–0°, 180°–240°E), and all tropical oceans (15°N–15°S), respectively. While application of this POD to data from these different geographical regions produces results that appear remarkably similar, Inoue et al. (2021) highlight that the primary balances and imbalances of processes driving convective cycles in the CP differ from those in the IOWP, suggesting that these geographical regions should be considered separately.

REFERENCES

Adames, Á. F., and D. Kim, 2016: The MJO as a dispersive, convectively coupled moisture wave: Theory and observations. *J. Atmos. Sci.*, **73**, 913–941, https://doi.org/10.1175/JAS-D-15-0170.1.

——, and Y. Ming, 2018: Interactions between water vapor and potential vorticity in synoptic-scale monsoonal disturbances: Moisture vortex instability. *J. Atmos. Sci.*, **75**, 2083–2106, https://doi.org/10.1175/JAS-D-17-0310.1.

——, S. W. Powell, F. Ahmed, V. C. Mayta, and J. D. Neelin, 2021: Tropical precipitation evolution in a buoyancy-budget framework. *J. Atmos. Sci.*, **78**, 509–528, https://doi.org/10.1175/JAS-D-20-0074.1.

Ahmed, F., and C. Schumacher, 2015: Convective and stratiform components of the precipitation-moisture relationship. *Geophys. Res. Lett.*, **42**, 10 453–10 462, https://doi.org/10.1002/2015GL066957.

——, and ——, 2017: Geographical differences in the tropical precipitation-moisture relationship and rain intensity onset. *Geophys. Res. Lett.*, **44**, 1114–1122, https://doi.org/10.1002/2016GL071980.

——, and J. D. Neelin, 2018: Reverse engineering the tropical precipitation–buoyancy relationship. *J. Atmos. Sci.*, **75**, 1587–1608, https://doi.org/10.1175/JAS-D-17-0333.1.

——, and ——, 2021: A process-oriented diagnostic to assess precipitation-thermodynamic relations and application to CMIP6 models. *Geophys. Res. Lett.*, **48**, e2021GL094108, https://doi.org/10.1029/2021GL094108.

——, Á. F. Adames, and J. D. Neelin, 2020: Deep convective adjustment of temperature and moisture. *J. Atmos. Sci.*, **77**, 2163–2186, https://doi.org/10.1175/JAS-D-19-0227.1.

Ahn, M.-S., D. Kim, K. R. Sperber, I.-S. Kang, E. Maloney, D. Waliser, and H. Hendon, 2017: MJO simulation in CMIP5 climate models: MJO skill metrics and process-oriented diagnosis. *Climate Dyn.*, **49**, 4023–4045, https://doi.org/10.1007/s00382-017-3558-4.

Arakawa, A., 2004: The cumulus parameterization problem: Past, present, and future. *J. Climate*, **17**, 2493–2525, https://doi.org/10.1175/1520-0442(2004)017<2493:RATCPP>2.0.CO;2.

——, and W.H. Schubert, 1974: Interaction of a cumulus cloud ensemble with the large-scale environment, part I. *J. Atmos. Sci.*, **31**, 674–701, https://doi.org/10.1175/1520-0469(1974)031<0674:IOACCE>2.0.CO;2.

Arnold, N. P., and D. A. Randall, 2015: Global-scale convective aggregation: Implications for the Madden-Julian oscillation. *J. Adv. Model. Earth Syst.*, **7**, 1499–1518, https://doi.org/10.1002/2015MS000498.

Back, L., and C. Bretherton, 2006: Geographic variability in the export of moist static energy and vertical motion profiles in the tropical Pacific. *Geophys. Res. Lett.*, **33**, L17810, https://doi.org/10.1029/2006GL026672.

Basha, G., and M. V. Ratnam, 2009: Identification of atmospheric boundary layer height over a tropical station using high-resolution radiosonde refractivity profiles: Comparison with GPS radio occultation measurements. *J. Geophys. Res.*, **114**, D16101, https://doi.org/10.1029/2008JD011692.

Bergemann, M., and C. Jakob, 2016: How important is tropospheric humidity for coastal rainfall in the tropics? *Geophys. Res. Lett.*, **43**, 5860–5868, https://doi.org/10.1002/2016GL069255.

Bjerknes, J., 1966: A possible response of the atmospheric Hadley circulation to equatorial anomalies of ocean temperature. *Tellus*, **18**, 820–829, https://doi.org/10.3402/tellusa.v18i4.9712.

Bony, S., and Coauthors, 2015: Clouds, circulation and climate sensitivity. *Nat. Geosci.*, **8**, 261–268, https://doi.org/10.1038/ngeo2398.

——, A. Semie, R. Kramer, B. Soden, A. Tompkins, and K. Emanuel, 2020: Observed modulation of the tropical radiation budget by deep convective organization and lower-tropospheric stability. *AGU Adv.*, **1**, e2019AV000155, https://doi.org/10.1029/2019AV000155.

Branstator, G., 2014: Long-lived response of the midlatitude circulation and storm tracks to pulses of tropical heating. *J. Climate*, **27**, 8809–8826, https://doi.org/10.1175/JCLI-D-14-00312.1.

Bretherton, C. S., M. E. Peters, and L. E. Back, 2004: Relationships between water vapor path and precipitation over the tropical oceans. *J. Climate*, **17**, 1517–1528, https://doi.org/10.1175/1520-0442(2004)017<1517:RBWVPA>2.0.CO;2.

——, P.N. Blossey, and M. Khairoutdinov, 2005: An energy-balance analysis of deep convective self-aggregation above uniform SST. *J. Atmos. Sci.*, **62**, 4273–4292, https://doi.org/10.1175/JAS3614.1.

Chen, S. S., and R. A. Houze Jr., 1997: Diurnal variation and life-cycle of deep convective systems over the tropical Pacific warm pool. *Quart. J. Roy. Meteor. Soc.*, **123**, 357–388, https://doi.org/10.1002/qj.49712353806.

Chikira, M., 2014: Eastward-propagating intraseasonal oscillation represented by Chikira–Sugiyama cumulus parameterization. Part II: Understanding moisture variation under weak temperature gradient balance. *J. Atmos. Sci.*, **71**, 615–639, https://doi.org/10.1175/JAS-D-13-038.1.

Dee, D., and Coauthors, 2011: The ERA-Interim reanalysis: Configuration and performance of the data assimilation system. *Quart. J. Roy. Meteor. Soc.*, **137**, 553–597, https://doi.org/10.1002/qj.828.

Dias, J., and G. N. Kiladis, 2019: The influence of tropical forecast errors on higher latitude predictions. *Geophys. Res. Lett.*, **46**, 4450–4459, https://doi.org/10.1029/2019GL082812.

——, S. N. Tulich, M. Gehne, and G. N. Kiladis, 2021: Tropical origins of weeks 2–4 forecasts errors during Northern Hemisphere cool season. *Mon. Wea. Rev.*, **149**, 2975–2991, https://doi.org/10.1175/MWR-D-21-0020.1.

Durre, I., R. S. Vose, and D. B. Wuertz, 2006: Overview of the integrated global radiosonde archive. *J. Climate*, **19**, 53–68, https://doi.org/10.1175/JCLI3594.1.

——, X. Yin, R. S. Vose, S. Applequist, and J. Arnfield, 2018: Enhancing the data coverage in the Integrated Global Radiosonde Archive. *J. Atmos. Oceanic Technol.*, **35**, 1753–1770, https://doi.org/10.1175/JTECH-D-17-0223.1.

Emanuel, K., 1993: The effect of convective response time on WISHE modes. *J. Atmos. Sci.*, **50**, 1763–1776, https://doi.org/10.1175/1520-0469(1993)050<1763:TEOCRT>2.0.CO;2.

——, J. D. Neelin, and C. S. Bretherton, 1994: On large-scale circulations in convecting atmospheres. *Quart. J. Roy. Meteor. Soc.*, **120**, 1111–1143, https://doi.org/10.1002/qj.49712051902.

Fuchs-Stone, Ž., D. J. Raymond, and S. Sentić, 2020: OTREC2019: Convection over the east Pacific and southwest Caribbean. *Geophys. Res. Lett.*, **47**, e2020GL087564, https://doi.org/10.1029/2020GL087564.

Funk, A., C. Schumacher, and J. Awaka, 2013: Analysis of rain classifications over the tropics by version 7 of the TRMM PR 2A23 algorithm. *J. Meteor. Soc. Japan*, **91**, 257–272, https://doi.org/10.2151/jmsj.2013-302.

Hartmann, D. L., H. H. Hendon, and R. A. Houze Jr., 1984: Some implications of the mesoscale circulations in tropical cloud clusters for large-scale dynamics and climate. *J. Atmos. Sci.*, **41**, 113–121, https://doi.org/10.1175/1520-0469(1984)041<0113:SIOTMC>2.0.CO;2.

Hersbach, H., and Coauthors, 2020: The ERA5 global reanalysis. *Quart. J. Roy. Meteor. Soc.*, **146**, 1999–2049, https://doi.org/10.1002/qj.3803.

Ho, S., X. Zhou, Y.-H. Kuo, D. Hunt, and J. Wang, 2010: Global evaluation of radiosonde water vapor systematic biases using GPS radio occultation from cosmic and ECMWF analysis. *Remote Sens.*, **2**, 1320–1330, https://doi.org/10.3390/rs2051320.

——, and Coauthors, 2020: The COSMIC/FORMOSAT-3 radio occultation mission after 12 years: Accomplishments, remaining challenges, and potential impacts of COSMIC-2. *Bull. Amer. Meteor. Soc.*, **101**, E1107–E1136, https://doi.org/10.1175/BAMS-D-18-0290.1.

Hollars, S., Q. Fu, J. Comstock, and T. Ackerman, 2004: Comparison of cloud-top height retrievals from ground-based 35 GHZ MMCR and GMS-5 satellite observations at ARM TWP MANUS site. *Atmos. Res.*, **72**, 169–186, https://doi.org/10.1016/j.atmosres.2004.03.015.

Holloway, C. E., and J. D. Neelin, 2009: Moisture vertical structure, column water vapor, and tropical deep convection. *J. Atmos. Sci.*, **66**, 1665–1683, https://doi.org/10.1175/2008JAS2806.1.

Hoskins, B. J., and D. J. Karoly, 1981: The steady linear response of a spherical atmosphere to thermal and orographic forcing. *J. Atmos. Sci.*, **38**, 1179–1196, https://doi.org/10.1175/1520-0469(1981)038<1179:TSLROA>2.0.CO;2.

Houze, R. A., Jr., 1982: Cloud clusters and large-scale vertical motions in the tropics. *J. Meteor. Soc. Japan*, **60**, 396–410, https://doi.org/10.2151/jmsj1965.60.1_396.

Huffman, G. J., and Coauthors, 2007: The TRMM Multisatellite Precipitation Analysis (TMPA): Quasi-global, multiyear, combined-sensor precipitation estimates at fine scales. *J. Hydrometeor.*, **8**, 38–55, https://doi.org/10.1175/JHM560.1.

Inoue, K., and L. E. Back, 2017: Gross moist stability analysis: Assessment of satellite-based products in the GMS plane. *J. Atmos. Sci.*, **74**, 1819–1837, https://doi.org/10.1175/JAS-D-16-0218.1.

——, Á. F. Adames, and K. Yasunaga, 2020: Vertical velocity profiles in convectively coupled equatorial waves and MJO: New diagnoses of vertical velocity profiles in the wavenumber–frequency domain. *J. Atmos. Sci.*, **77**, 2139–2162, https://doi.org/10.1175/JAS-D-19-0209.1.

——, M. Biasutti, and A. M. Fridlind, 2021: Evidence that horizontal moisture advection regulates the ubiquitous amplification of rainfall variability over tropical oceans. *J. Atmos. Sci.*, **78**, 529–547, https://doi.org/10.1175/JAS-D-20-0201.1.

Jiang, X., and Coauthors, 2015: Vertical structure and physical processes of the Madden-Julian oscillation: Exploring key model physics in climate simulations. *J. Geophys. Res. Atmos.*, **120**, 4718–4748, https://doi.org/10.1002/2014JD022375.

——, and Coauthors, 2020: Fifty years of research on the Madden-Julian oscillation: Recent progress, challenges, and perspectives. *J. Geophys. Res. Atmos.*, **125**, e2019JD030911, https://doi.org/10.1029/2019JD030911.

Johnson, R. H., T. M. Rickenbach, S. A. Rutledge, P. E. Ciesielski, and W. H. Schubert, 1999: Trimodal characteristics of tropical convection. *J. Climate*, **12**, 2397–2418, https://doi.org/10.1175/1520-0442(1999)012<2397:TCOTC>2.0.CO;2.

——, P. E. Ciesielski, J. H. Ruppert Jr., and M. Katsumata, 2014: Sounding-based thermodynamic budgets for DYNAMO. *J. Atmos. Sci.*, **72**, 598–622, https://doi.org/10.1175/JAS-D-14-0202.1.

Khouider, B., and A. J. Majda, 2006: A simple multicloud parameterization for convectively coupled tropical waves. Part I: Linear analysis. *J. Atmos. Sci.*, **63**, 1308–1323, https://doi.org/10.1175/JAS3677.1.

——, and ——, 2008: Multicloud models for organized tropical convection: Enhanced congestus heating. *J. Atmos. Sci.*, **65**, 895–914, https://doi.org/10.1175/2007JAS2408.1.

Kiladis, G. N., M. C. Wheeler, P. T. Haertel, K. H. Straub, and P.E. Roundy, 2009: Convectively coupled equatorial waves. *Rev. Geophys.*, **47**, RG2003, https://doi.org/10.1029/2008RG000266.

Kingsmill, D. E., and R. A. Houze Jr., 1999: Thermodynamic characteristics of air flowing into and out of precipitating convection over the west Pacific warm pool. *Quart. J. Roy. Meteor. Soc.*, **125**, 1209–1229, https://doi.org/10.1002/qj.1999.49712555606.

Kobayashi, S., and Coauthors, 2015: The JRA-55 Reanalysis: General specifications and basic characteristics. *J. Meteor. Soc. Japan*, **93**, 5–48, https://doi.org/10.2151/jmsj.2015-001.

Kuang, Z., 2008: A moisture-stratiform instability for convectively coupled waves. *J. Atmos. Sci.*, **65**, 834–854, https://doi.org/10.1175/2007JAS2444.1.

——, 2010: Linear response functions of a cumulus ensemble to temperature and moisture perturbations and implications for the dynamics of convectively coupled waves. *J. Atmos. Sci.*, **67**, 941–962, https://doi.org/10.1175/2009JAS3260.1.

Kumar, V. V., C. Jakob, A. Protat, C. R. Williams, and P. T. May, 2015: Mass-flux characteristics of tropical cumulus clouds from wind profiler observations at Darwin, Australia. *J. Atmos. Sci.*, **72**, 1837–1855, https://doi.org/10.1175/JAS-D-14-0259.1.

Kursinski, E., G. Hajj, J. Schofield, R. Linfield, and K. R. Hardy, 1997: Observing Earth's atmosphere with radio occultation measurements using the global positioning system. *J. Geophys. Res.*, **102**, 23 429–23 465, https://doi.org/10.1029/97JD01569.

Mapes, B. E., 2000: Convective inhibition, subgrid-scale triggering energy, and stratiform instability in a toy tropical wave model. *J. Atmos. Sci.*, **57**, 1515–1535, https://doi.org/10.1175/1520-0469(2000)057<1515:CISSTE>2.0.CO;2.

——, and R. A. Houze Jr., 1993: Cloud clusters and superclusters over the oceanic warm pool. *Mon. Wea. Rev.*, **121**, 1398–1416, https://doi.org/10.1175/1520-0493(1993)121<1398:CCASOT>2.0.CO;2.

——, S. Tulich, J. Lin, and P. Zuidema, 2006: The mesoscale convection life cycle: Building block or prototype for large-scale tropical waves? *Dyn. Atmos. Oceans*, **42**, 3–29, https://doi.org/10.1016/j.dynatmoce.2006.03.003.

Martin, S. T., and Coauthors, 2016: Introduction: Observations and modeling of the Green ocean Amazon (GoAmazon2014/5). *Atmos. Chem. Phys.*, **16**, 4785–4797, https://doi.org/10.5194/acp-16-4785-2016.

McGee, C. J., and S. C. Van den Heever, 2014: Latent heating and mixing due to entrainment in tropical deep convection. *J. Atmos. Sci.*, **71**, 816–832, https://doi.org/10.1175/JAS-D-13-0140.1.

Mechem, D. B., R. A. Houze Jr., and S. S. Chen, 2002: Layer inflow into precipitating convection over the western tropical Pacific. *Quart. J. Roy. Meteor.*, **128**, 1997–2030, https://doi.org/10.1256/003590002320603502.

Neelin, J. D., and I. M. Held, 1987: Modeling tropical convergence based on the moist static energy budget. *Mon. Wea. Rev.*, **115**, 3–12, https://doi.org/10.1175/1520-0493(1987)115<0003:MTCBOT>2.0.CO;2.

——, O. Peters, J. W.-B. Lin, K. Hales, and C. E. Holloway, 2008: Rethinking convective quasi-equilibrium: Observational constraints for stochastic convective schemes in climate models. *Philos. Trans. Roy. Soc.*, **366**, 2579–2602, https://doi.org/10.1098/rsta.2008.0056.

——, ——, and K. Hales, 2009: The transition to strong convection. *J. Atmos. Sci.*, **66**, 2367–2384, https://doi.org/10.1175/2009JAS2962.1.

Nicholls, S., and M. A. Lemone, 1980: The fair weather boundary layer in GATE: The relationship of subcloud fluxes and structure to the distribution and enhancement of cumulus clouds. *J. Atmos. Sci.*, **37**, 2051–2067, https://doi.org/10.1175/1520-0469(1980)037<2051:TFWBLI>2.0.CO;2.

Peters, O., and J. D. Neelin, 2006: Critical phenomena in atmospheric precipitation. *Nat. Phys.*, **2**, 393–396, https://doi.org/10.1038/nphys314.

Pincus, R., A. Beljaars, S. A. Buehler, G. Kirchengast, F. Ladstaedter, and J. S. Whitaker, 2017: The representation of tropospheric water vapor over low-latitude oceans in (re-) analysis: Errors, impacts, and the ability to exploit current and prospective observations. *Surv. Geophys.*, **38**, 1399–1423, https://doi.org/10.1007/s10712-017-9437-z.

Poli, P., S. Healy, and D. Dee, 2010: Assimilation of global positioning system radio occultation data in the ECMWF ERA-Interim reanalysis. *Quart. J. Roy. Meteor. Soc.*, **136**, 1972–1990, https://doi.org/10.1002/qj.722.

Powell, S. W., R. A. Houze Jr., and S. R. Brodzik, 2016: Rainfall-type categorization of radar echoes using polar coordinate reflectivity data. *J. Atmos. Oceanic Technol.*, **33**, 523–538, https://doi.org/10.1175/JTECH-D-15-0135.1.

Raymond, D. J., 1995: Regulation of moist convection over the west Pacific warm pool. *J. Atmos. Sci.*, **52**, 3945–3959, https://doi.org/10.1175/1520-0469(1995)052<3945:ROMCOT>2.0.CO;2.

——, 2000: Thermodynamic control of tropical rainfall. *Quart. J. Roy. Meteor. Soc.*, **126**, 889–898, https://doi.org/10.1002/qj.49712656406.

——, and M. J. Herman, 2011: Convective quasi-equilibrium reconsidered. *J. Adv. Model. Earth Syst.*, **3**, M08003, https://doi.org/10.1029/2011MS000079.

——, and Ž. Fuchs-Stone, 2021: Emergent properties of convection in OTREC and PREDICT. *J. Geophys. Res. Atmos.*, **126**, e2020JD033585, https://doi.org/10.1029/2020JD033585.

——, G. Raga, C. S. Bretherton, J. Molinari, C. López-Carrillo, and Ž. Fuchs, 2003: Convective forcing in the intertropical convergence zone of the eastern Pacific. *J. Atmos. Sci.*, **60**, 2064–2082, https://doi.org/10.1175/1520-0469(2003)060<2064:CFITIC>2.0.CO;2.

——, S. L. Sessions, A. H. Sobel, and Ž. Fuchs, 2009: The mechanics of gross moist stability. *J. Adv. Model. Earth Syst.*, **1**, 9, https://doi.org/10.3894/JAMES.2009.1.9.

——, Ž. Fuchs, S. Gjorgjievska, and S. Sessions, 2015: Balanced dynamics and convection in the tropical troposphere. *J. Adv. Model. Earth Syst.*, **7**, 1093–1116, https://doi.org/10.1002/2015MS000467.

Ren, P., D. Kim, M.-S. Ahn, D. Kang, and H.-L. Ren, 2021: Intercomparison of MJO column moist static energy and water vapor budget among six modern reanalysis products. *J. Climate*, **34**, 2977–3001, https://doi.org/10.1175/JCLI-D-20-0653.1.

Retsch, M., C. Jakob, and M. Singh, 2020: Assessing convective organization in tropical radar observations. *J. Geophys. Res. Atmos.*, **125**, e2019JD031801, https://doi.org/10.1029/2019JD031801.

Rushley, S., D. Kim, C. Bretherton, and M.-S. Ahn, 2018: Reexamining the nonlinear moisture-precipitation relationship over the tropical oceans. *Geophys. Res. Lett.*, **45**, 1133–1140, https://doi.org/10.1002/2017GL076296.

Sahany, S., J. D. Neelin, K. Hales, and R. B. Neale, 2012: Temperature–moisture dependence of the deep convective transition as a constraint on entrainment in climate models. *J. Atmos. Sci.*, **69**, 1340–1358, https://doi.org/10.1175/JAS-D-11-0164.1.

Sardeshmukh, P. D., and B. J. Hoskins, 1988: The generation of global rotational flow by steady idealized tropical divergence. *J. Atmos. Sci.*, **45**, 1228–1251, https://doi.org/10.1175/1520-0469(1988)045<1228:TGOGRF>2.0.CO;2.

Schiro, K. A., and J. D. Neelin, 2019: Deep convective organization, moisture vertical structure, and convective transition using deep-inflow mixing. *J. Atmos. Sci.*, **76**, 965–987, https://doi.org/10.1175/JAS-D-18-0122.1.

——, F. Ahmed, S. E. Giangrande, and J. D. Neelin, 2018: GoAmazon2014/5 campaign points to deep-inflow approach to deep convection across scales. *Proc. Natl. Acad. Sci. USA*, **115**, 4577–4582, https://doi.org/10.1073/pnas.1719842115.

——, S. C. Sullivan, Y.-H. Kuo, H. Su, P. Gentine, G. S. Elsaesser, J. H. Jiang, and J. D. Neelin, 2020: Environmental controls on tropical mesoscale convective system precipitation intensity. *J. Atmos. Sci.*, **77**, 4233–4249, https://doi.org/10.1175/JAS-D-20-0111.1.

Schröder, M., M. Lockhoff, J. M. Forsythe, H. Q. Cronk, T. H. Vonder Haar, and R. Bennartz, 2016: The GEWEX water vapor assessment: Results from intercomparison, trend, and homogeneity analysis of total column water vapor. *J. Appl. Meteor. Climatol.*, **55**, 1633–1649, https://doi.org/10.1175/JAMC-D-15-0304.1.

Schumacher, C., R. A. Houze Jr., and I. Kraucunas, 2004: The tropical dynamical response to latent heating estimates derived from the TRMM Precipitation Radar. *J. Atmos. Sci.*, **61**, 1341–1358, https://doi.org/10.1175/1520-0469(2004)061<1341:TTDRTL>2.0.CO;2.

Sobel, A., S. Wang, and D. Kim, 2014: Moist static energy budget of the MJO during DYNAMO. *J. Atmos. Sci.*, **71**, 4276–4291, https://doi.org/10.1175/JAS-D-14-0052.1.

Stevens, B., and Coauthors, 2019: DYAMOND: The Dynamics of the Atmospheric general circulation Modeled On Non-hydrostatic Domains. *Prog. Earth Planet. Sci.*, **6**, 61, https://doi.org/10.1186/s40645-019-0304-z.

Thayer-Calder, K., and D. A. Randall, 2009: The role of convective moistening in the Madden–Julian oscillation. *J. Atmos. Sci.*, **66**, 3297–3312, https://doi.org/10.1175/2009JAS3081.1.

Thompson, E. J., S. A. Rutledge, B. Dolan, M. Thurai, and V. Chandrasekar, 2018: Dual-polarization radar rainfall estimation over tropical oceans. *J. Appl. Meteor. Climatol.*, **57**, 755–775, https://doi.org/10.1175/JAMC-D-17-0160.1.

Thompson, R. M., Jr., S. W. Payne, E. E. Recker, and R. J. Reed, 1979: Structure and properties of synoptic-scale wave disturbances in the intertropical convergence zone of the eastern Atlantic. *J. Atmos. Sci.*, **36**, 53–72, https://doi.org/10.1175/1520-0469(1979)036<0053:SAPOSS>2.0.CO;2.

Tulich, S. N., and B. E. Mapes, 2010: Transient environmental sensitivities of explicitly simulated tropical convection. *J. Atmos. Sci.*, **67**, 923–940, https://doi.org/10.1175/2009JAS3277.1.

Wing, A. A., and K. A. Emanuel, 2014: Physical mechanisms controlling self-aggregation of convection in idealized numerical modeling simulations. *J. Adv. Model. Earth Syst.*, **6**, 59–74, https://doi.org/10.1002/2013MS000269.

Wolding, B. O., and E. D. Maloney, 2015: Objective diagnostics and the Madden–Julian oscillation. Part II: Application to moist static energy and moisture budgets. *J. Climate*, **28**, 7786–7808, https://doi.org/10.1175/JCLI-D-14-00689.1.

——, ——, and M. Branson, 2016: Vertically resolved weak temperature gradient analysis of the Madden-Julian oscillation in SP-CESM. *J. Adv. Model. Earth Syst.*, **8**, 1586–1619, https://doi.org/10.1002/2016MS000724.

——, J. Dias, G. Kiladis, F. Ahmed, S. W. Powell, E. Maloney, and M. Branson, 2020a: Interactions between moisture and tropical convection. Part I: The coevolution of moisture and convection. *J. Atmos. Sci.*, **77**, 1783–1799, https://doi.org/10.1175/JAS-D-19-0225.1.

——, ——, ——, E. Maloney, and M. Branson, 2020b: Interactions between moisture and tropical convection. Part II: The convective coupling of equatorial waves. *J. Atmos. Sci.*, **77**, 1801–1819, https://doi.org/10.1175/JAS-D-19-0226.1.

Xie, F., D. Wu, C. Ao, A. Mannucci, and E. Kursinski, 2012: Advances and limitations of atmospheric boundary layer observations with GPS occultation over southeast Pacific Ocean. *Atmos. Chem. Phys.*, **12**, 903–918, https://doi.org/10.5194/acp-12-903-2012.

Yasunaga, K., S. Yokoi, K. Inoue, and B. E. Mapes, 2019: Space–time spectral analysis of the moist static energy budget equation. *J. Climate*, **32**, 501–529, https://doi.org/10.1175/JCLI-D-18-0334.1.

Yoneyama, K., C. Zhang, and C. N. Long, 2013: Tracking pulses of the Madden–Julian oscillation. *Bull. Amer. Meteor. Soc.*, **94**, 1871–1891, https://doi.org/10.1175/BAMS-D-12-00157.1.

Zhang, C., 2005: Madden-Julian oscillation. *Rev. Geophys.*, **43**, RG2003, https://doi.org/10.1029/2004RG000158.

——, and S. M. Hagos, 2009: Bi-modal structure and variability of large-scale diabatic heating in the tropics. *J. Atmos. Sci.*, **66**, 3621–3640, https://doi.org/10.1175/2009JAS3089.1.

Zipser, E. J., 2003: Some views on "hot towers" after 50 years of tropical field programs and two years of TRMM data. *Cloud Systems, Hurricanes, and the Tropical Rainfall Measuring Mission (TRMM)*, *Meteor. Monogr.*, No. 29, Amer. Meteor. Soc., 49–58, https://doi.org/10.1175/0065-9401(2003)029<0049:CSVOHT>2.0.CO;2.